博士論文

Theory of the Fulde–Ferrell–Larkin–Ovchinnikov State in Quasi-One-Dimensional Type-Ⅱ Superconductors

広島大学 大学院先端物質科学研究科

量子物質科学専攻

板橋 克美

Acknowledgments

I would like to express my gratitude to Professor Hiroshi Shimahara for his continued courteous guidance and numerous advice. I am indebted to Dr. Shingo Yonezawa and Professor Keita Kishigi for discussions and information. I would also like to express my sincere gratitude to Professor Katsuhiko Higuchi and Arata Tanaka for discussions and words of encouragement. I would also like to thank Dr. Kazuhiro Ito, Dr. Tomoaki Matsuzaki, Mr. Yuki Kono, and all members of the institute of theoretical physics for discussions and support.

Contents

Chapter 1

Introduction and Purpose

1.1 Overview

Recently, it has been suggested that a nonuniform superconducting state called the Fulde–Ferrell–Lakin–Ovchinnikov state (the FFLO state) may occur in exotic superconductors, such as heavy fermion and organic superconductors [1–3]. This state occurs when spin-polarization energy is large in clean type-II superconductors in strong magnetic fields [4, 5]. Therefore, the orbital pair-breaking effect needs to be weak. The FFLO state is induced by Cooper pairs with nonzero center-of-mass momenta $\boldsymbol{q}$. Hence, because $\boldsymbol{q} \neq 0$, the order parameter of this state spatially oscillates.

The FFLO state had not been observed for a long time for the following reasons. Because the impurity scattering destroys the FFLO state [6, 7], the sample needs to be clean for the occurrence of the FFLO state. Therefore, in conventional alloy type-II superconductors, the FFLO state does not occur because they contain impurities that make the coherence length ξ small. In addition, in alloy superconductors, the orbital pair-breaking effect is strong. This effect can be weak, if the magnetic field is applied in the direction parallel to the film metal superconductors. However, the FFLO state was not observed. A possible reason is that the magnetic field was not precisely parallel to the film [8].

In contrast to conventional alloy superconductors, the exotic superconductors can be clean type-II superconductors, and simultaneously, the heavy effective mass and/or narrow band width of these superconductors can suppress the orbital pair-breaking effect. Therefore, the FFLO state can occur in the exotic superconductors [2,3].

In addition, quasi-low-dimensional structures of these superconductors are favorable to the FFLO state because of a stabilization effect that originates from the Fermi surface structure, which is analogous to the nesting effect for the charge density wave and spin density wave (CDW and SDW) [9–11]. The pairing anisotropy in exotic superconductors also contributes to the nesting effect for the FFLO state.

There is another mechanism that stabilizes the FFLO state, when the singlet and triplet order parameters coexist. This effect is called the order-parameter mixing effect [12,13].

In Section 1.2 of this chapter, we review the fundamental properties of the FFLO state and these stabilization mechanisms, then we review the possibility of the FFLO state in organic superconductors.

In the quasi-one-dimensional (Q1D) organic compound $(\mathrm{TMTSF})_2\mathrm{ClO}_4$, where TMTSF stands for tetramethyltetraselenafulvalene, Yonezawa et al. observed the angular dependence of the onset transition temperature $T_{\mathrm{c}}^{\mathrm{onset}}(\phi)$, where ϕ denotes the angle between the in-plane magnetic field $\boldsymbol{H}$ and the crystal a-axis [14,15]. They found that the principal axis of $T_{\mathrm{c}}^{\mathrm{onset}}(\phi)$ changed at a high field, and argued that this may be related to the possible emergence of the FFLO state. In this compound, the FFLO state and the anisotropic superconductivity have been studied theoretically and experimentally by many authors, as reviewed in Section 1.3.

These theoretical and experimental studies motivated us to examine the FFLO state in Q1D anisotropic superconductors. In particular, we focus on the nesting effect and the order-parameter mixing effect.

This thesis is organized as follows.

In Chapter 2, we review the superconductivity in the magnetic field. In $(\mathrm{TMTSF})_2X$ ($X = \mathrm{ClO}_4, \mathrm{PF}_6, \mathrm{etc.}$), it has been suggested that the orbital pair-breaking effect is not negligible, although this effect is sufficiently weak. We review the orbital and paramagnetic pair-breaking effects in type-II superconductors and the FFLO state in the presence of a weak orbital pair-breaking effect [8, 16].

In Chapter 3, we survey the anisotropic superconductivity in Q1D systems. In these systems, various pairing interactions have been theoretically discussed by many authors [17–19]. We assume pairing symmetries according to the studies reviewed in this chapter.

In Chapter 4, we formulate the upper critical field and the transition temperature of the FFLO state in Q1D systems. We also explain assumptions in the thesis, such as that on the orbital pair-breaking effect.

In Chapter 5, we apply the theory to $(\mathrm{TMTSF})_2\mathrm{ClO}_4$. For a close comparison to the experimental results, we adopt the energy dispersion, hopping integrals, and lattice parameters that are realistic for $(\mathrm{TMTSF})_2\mathrm{ClO}_4$.

In Chapter 6, we examine the in-plane-magnetic-field-direction dependence of the stability of the FFLO state. We compare the theoretical results with the optimum direction of $\boldsymbol{H}$ observed at high fields. We examine the relation between the optimum direction and hopping parameters. Lastly, we examine the mixing effect for the FFLO state in Q1D systems.

In Chapter 7, we discuss the results and conclude the thesis.

1.2 The FFLO state

In this section, we review the fundamental properties of the FFLO state and its stabilization mechanisms.

In conventional superconductors, the superconductivity is induced by the Cooper pairs of two electrons with $\boldsymbol{k} \uparrow$ and $-\boldsymbol{k} \downarrow$. In this thesis, we refer to such a superconducting state as the BCS state. In the absence of the orbital pair-breaking effect, the BCS state is broken into the normal state when the magnetic field reaches a value so that the condensation energy coincides with the spin polarization energy. This field, which is called the Pauli paramagnetic limit (Chandrasekhar-Clogston limit) [20], is expressed as $H_{\mathrm{P}} = \Delta_0/\mu_{\mathrm{e}}\sqrt{2}$, where Δ_0 and μ_{e} are the energy gap at the zero-field and the magnetic moment of the electron, respectively.

The FFLO state is induced by the Cooper pairs of two electrons with $\boldsymbol{k} \uparrow$ and $-\boldsymbol{k}+\boldsymbol{q} \downarrow$ near the Fermi surfaces splitted by the Zeeman energy as shown in Fig. 1.1.

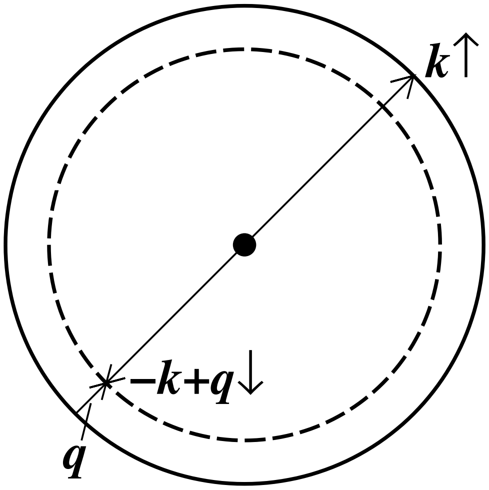

Figure 1.1: Schematic figure of the FFLO state. The solid and dashed curves show the Fermi surfaces of electrons with up and down spins, respectively.

In this state, the order parameter spatially oscillates as $\Delta_{\boldsymbol{q}}(\boldsymbol{R}) \propto \mathrm{e}^{i\boldsymbol{q}\cdot\boldsymbol{R}}$, where $\boldsymbol{R}$ is the center-of-mass coordinate. We refer to the spatial oscillation of the order parameter and the nonzero $\boldsymbol{q}$ as the FFLO modulation and the FFLO vector, respectively. Fulde and Ferrell examined the state expressed by $\Delta(\boldsymbol{R}) = \mathrm{e}^{i\boldsymbol{q}\cdot\boldsymbol{R}}\Delta_1$ [4]. Larkin and Ovchinnikov examined the state expressed by $\Delta(\boldsymbol{R}) = \cos(\boldsymbol{q}\cdot\boldsymbol{R})\Delta_1$ [5].

Because of this modulation, the condensation energy of the FFLO state is larger than that of the BCS state. However, if a gain in the spin polarization energy reduces the total energy, the FFLO state occurs. Therefore, the FFLO state can occur at high magnetic fields where the BCS state is suppressed when $H > H_{\mathrm{P}}$ as shown in Fig. 1.2 [9]. T^* denotes the tricritical temperature of the FFLO, BCS, and normal states. In the absence of the orbital pair-breaking effect, $T^* \approx 0.56T_{\mathrm{c}}^{(0)}$, where $T_{\mathrm{c}}^{(0)}$ is the zero-field transition temperature.

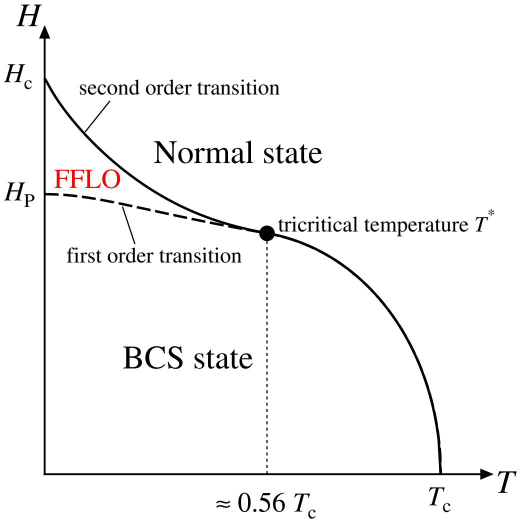

Figure 1.2: The H-T phase diagram in an isotropic two-dimensional system in the absence of the orbital pair-breaking effect [9].

If the orbital pair-breaking effect is stronger than the spin pair-breaking effect, the superconducting state cannot survive by the Pauli paramagnetic limit. Hence, it is required that the orbital pair-breaking effect is smaller than the spin pair-breaking effect. The organic superconductors are clean type-Ⅱ superconductors, and simultaneously, the orbital pair-breaking effect can be weak when the magnetic field is applied to the conductive plane.

The orbital pair-breaking effect is invariably present in type-Ⅱ superconductors. Gruenberg and Gunther examined the FFLO state in the presence of the orbital pair-breaking effect in isotropic three-dimensional systems [16]. They showed that the direction of the FFLO vector $\boldsymbol{q}$ is locked in that of the magnetic field $\boldsymbol{H}$ in the presence of a weak the orbital pair-breaking effect; i.e., $\boldsymbol{q} \parallel \boldsymbol{H}$.

1.2.1 Fermi surface nesting for the FFLO state

In this subsection, we review the nesting effect for the FFLO state [9–11,21–23]. In this state, there exist the characteristic FFLO vectors $\boldsymbol{q}$ analogous to the nesting vector $\boldsymbol{Q}$ in the CDW and SDW states. Therefore, for the FFLO state, the Fermi surface nesting effect can be introduced. To examine the nesting effect, it is useful to consider the overlap of the Fermi surface of the up spin electrons and the Fermi surface of the down spin electrons that is shifted by $\boldsymbol{q}$ (hereafter simply expressed as "the Fermi surfaces" at some subsequent instances below). In the following, we ignore the orbital pair-breaking effect. Figure 1.3 is a schematic figure of the Fermi surface nesting for the FFLO state.

In one-dimensional (1D) systems, the Fermi surfaces fully touch on a surface, where one of them is shifted by an appropriate $\boldsymbol{q}$, and nesting is perfect. Thus, the upper critical field of the FFLO state ($H_{\rm FFLO}$) diverges at $T \to 0$. It may appear that the FFLO state is most stable in 1D systems. However, in 1D systems, because the usual nesting instability induces the SDW or CDW at a higher transition

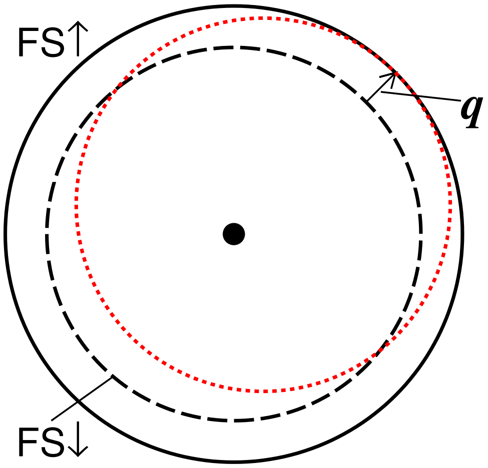

Figure 1.3: Schematic figure of the Fermi surface nesting for the FFLO state. The black solid and dashed curves show the Fermi surfaces of electrons with up and down spins, respectively. The red dotted curve shows the Fermi surface of electrons with down spin shifted by $\boldsymbol{q}$(small arrow).

temperature for realistic coupling constants, the superconducting transition hardly occurs.

On the other hand, in three-dimensional (3D) systems, the Fermi surfaces touch on a point or cross. When the Fermi surfaces cross, the nesting condition is better than touching on a point. In this condition, H_{FFLO} is slightly larger than H_{P}, and $H_{\mathrm{FFLO}}/H_{\mathrm{P}} = 1.075$ [4, 24].

In quasi-two-dimensional (Q2D) systems, the Fermi surfaces touch on a line in the 3D momentum space. In particular, in isotropic Q2D systems at $T = 0$, it has been shown that the length $|\boldsymbol{q}|$ is $2\mu_{\mathrm{e}}H/\Delta_0 v_{\mathrm{F}}$, where v_{F} is the Fermi velocity. In this case, $H_{\mathrm{FFLO}} = \sqrt{2}H_{\mathrm{P}}$. When the Fermi surfaces touch on a line, $\mathrm{d}H_{\mathrm{c}}/\mathrm{d}T < 0$ at $T = 0$, which means that the upper critical field shows up-turn at low temperatures [9]. Therefore, it is considered that Q2D systems in which the SDW and CDW transitions are suppressed must be most favorable to the FFLO state. The

(TMTSF)$_2X$ compounds are classified as Q2D systems in the sense that the Fermi surfaces are sufficiently warped enough to suppress the CDW and SDW. However, they are traditionally called Q1D organic superconductors because one of the hopping integrals is much larger than the others [21].

To clarify the nesting effect for the FFLO state in detail, Shimahara examined the nesting effect in a square lattice system in which shapes of the Fermi surface are changed by changing the hole density n_h [11]. It might be expected that the FFLO state is stabilized when the Fermi surface has a flat portion such as 1D systems. However, in reality, a round Fermi surface at $n_\mathrm{h} \approx 0.630$ provides the greatest stability for the FFLO state. At $n_\mathrm{h} \approx 0.630$, $H_\mathrm{c}(n_\mathrm{h})$ exhibits a sharp cusp and exceeds five times the Pauli paramagnetic limit. This sharp cusp is explained as follows. The difference between the Fermi surfaces can be expressed by

$$\Delta k_x^\mathrm{F}(k_y, \boldsymbol{q}) \equiv k_x^{\mathrm{F}\downarrow}(k_y - q_y) - k_x^{\mathrm{F}\uparrow}(k_y) + q_x, \tag{1.1}$$

where $k_x^{\mathrm{F}\sigma}(k_y)$ is the Fermi surface of σ spin. $\Delta k_x^\mathrm{F}(k_y, \boldsymbol{q})$ is expressed as $\Delta k_x^\mathrm{F}(k_y, \boldsymbol{q}) \propto (k_y - k_y^0)^n$ near $k_y = k_y^0(\boldsymbol{q})$ with an integer n. We have defined $k_y^0(\boldsymbol{q})$ by $\Delta k_x^\mathrm{F}(k_y^0(\boldsymbol{q}), \boldsymbol{q}) = 0$. When $n = 1$, it means that the nesting condition is crossing. The upper critical field is enhanced for $\boldsymbol{q}$ that gives $n = 2$, which implies that the Fermi surfaces touch on the line at $k_y = k_y^0(\boldsymbol{q})$. In a square lattice system at $n_\mathrm{h} \approx 0.630$, $n = 4$ for an appropriate $\boldsymbol{q}$, which results in the previously mentioned sharp cusp and extreme enhancement of $H_\mathrm{c}(n_\mathrm{h})$ [11]. Therefore, the nesting effect sensitively depends on the Fermi-surface structure. In addition, the structure of the gap function must be taken into account because the momentum dependence near the Fermi surfaces affects the nesting effect [10, 22, 23].

The enhancement of the upper critical field due to quasi-low-dimensionality is physically significant for the following reasons. The orbital pair-breaking effect reduces the upper critical field. In 3D systems, H_FFLO exceeds H_P slightly; however, the above effect reduces the upper critical field. Hence, the FFLO state could be suppressed ($H_{\mathrm{FFLO}} < H_{\mathrm{P}}$). When the enhancement of the internal magnetic field due to Coulomb repulsive is considered, the upper critical field becomes less than the Pauli paramagnetic limit. Therefore, for the FFLO state to exist stably, contributions of the nesting effect and the order-parameter mixing effect are significant.

1.2.2 Order-parameter mixing effect

In this subsection, we review the order-parameter mixing effect for the FFLO state. In exotic superconductors, various mechanisms of the pairing interactions have been discussed. For organic superconductors, because the superconducting phase appears in proximately to the antiferromagnetic phase in p-H-T phase diagrams [25, 26], the pairing interaction mediated by antiferromagnetic fluctuations is examined by many authors. It has been suggested that such a pairing interaction contains both singlet and triplet attractive channels [19].

In the FFLO state, the spatial symmetry in the real space is reduced because of the FFLO vector $\boldsymbol{q}$ ($\neq 0$), and simultaneously, the rotational symmetry in the spin space is reduced because of the magnetic field. In the FFLO state, the singlet and triplet order parameters are mixed.

When it is supposed that dominant singlet pairing mixes with subdominant triplet pairing, the upper critical field in the presence of the order-parameter mixing effect is larger than that in the pure singlet state [12, 13]. Besides, the tricritical temperature T^* is larger than $0.56T_{\mathrm{c}}^{(0)}$, which is the tricritical temperature in the pure singlet state. Therefore, the FFLO state is stabilized by the order-parameter mixing effect. Hereafter, we simply express this effect as the mixing effect. Figure 1.4 shows the H-T phase diagram in the presence of the mixing effect for the FFLO state [13].

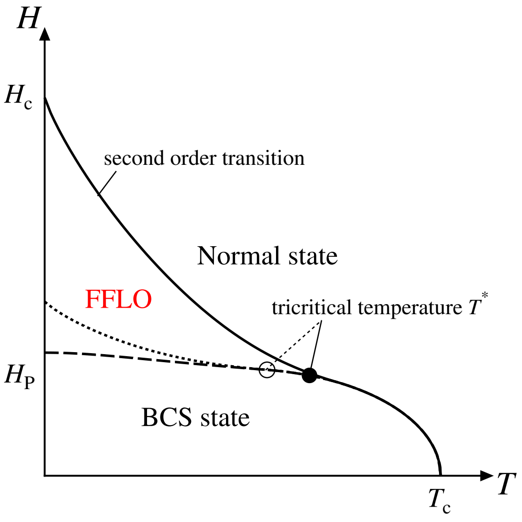

Figure 1.4: The H-T phase diagram in the presence of the mixing effect for the FFLO state in an isotropic two-dimensional system [13]. The dotted curve shows the second-order transition curve between the FFLO and normal states in the absence of the mixing effect. The open and closed circles are the tricritical temperature in the absence and presence of the mixing effect, respectively.

The mixing effect in 3D and 2D systems has been examined by Matsuo et al. and Shimahara [12, 13]. It has been shown that the tricritical temperature T^* depends on

$$G = \log \frac{T_{c1}^{(0)}}{T_{c0}^{(0)}} = \frac{1}{g_1 N_1(0)} - \frac{1}{g_0 N_0(0)}, \tag{1.2}$$

where $N_1(0)$ and g_1 ($N_0(0)$ and g_0) are the density of state at the Fermi energy and coupling constant of the singlet (triplet) pairing symmetries, respectively. For example, in the s-p mixing FFLO state, $T^* \approx 0.67 T_{c0}^{(0)}$ and $T^* \approx 0.74 T_{c0}^{(0)}$ for $G = \log 0.01$ and $G = \log 0.1$, respectively [12]. Therefore, it has been shown that in these systems, the FFLO state is stabilized by the mixing effect, even if the triplet pairing interaction very weak.

1.2.3 The FFLO state in organic superconductors

In this subsection, we review previous researches on the FFLO state in organic superconductors. The narrow band width of these superconductors gives quasi-low-dimensional structures and the suppression of the orbital pair-breaking effect, which are favorable to the FFLO state. Hence, when the magnetic field is applied to the conductive plane in organic superconductors, the FFLO state can occur.

The occurrence of the FFLO state is suggested in the Q2D organic compound κ-(BEDT-TTF)$_2$Cu(NCS)$_2$ [27], where (BEDT-TTF) stands for bis(ethylenedithio)tetrathiafulvalene. Lortz and Bergk et al. determined the H-T phase diagrams from experimental results of the specific heat and the magnetic torque. Their study suggested that the superconducting phase in high magnetic fields is the FFLO phase [28, 29]. Agosta et al. also suggested that release and absorb of latent heat relate to the FFLO state, from the calorimetric measurement [30]. NMR spectra measured by Wright et al. indicated that the phase transition within the superconducting state is Zeeman driven [31]. In addition, Mayaffre et al. suggested that the Andreev bound state observed in NMR measurement relates to the FFLO state [32].

In the Q2D organic compound λ-(BETS)$_2$FeCl$_4$, where BETS stands for bis(ethylenedithio)tetraselenafulvalene, Uji et al. carried out the resistance measurement in the field-induced superconducting phase, and obtained a characteristic dip structure suggesting the FFLO state [26, 33]. In addition, in the magnetic torque measurement, they obtained the result suggesting the FFLO state [34]. Shimahara reproduced the temperature dependence of the upper critical field in the field-induced superconducting phase by taking into account the combination of the Jaccarino-Peter mechanism and the FFLO state in the presence of the mixing effect [35]. In a similar compound λ-(BETS)$_2$GaCl$_4$, Tanater et al. measured the thermal conductivity in the in-plane magnetic field, and obtained several results consistent with theoretical predictions for the FFLO state [36].

Uji et al. also suggested the occurrence of the FFLO state in the Q2D compound β''-(BEDT-TTF)$_4$[(H$_3$O)Ga(C$_2$O$_4$)$_3$]C$_6$H$_5$NO$_2$ from the resistance and the magnetic torque measurement [37]. In the similar compound β''-(BEDT-TTF)$_2$SF$_5$CH$_2$CF$_2$SO$_3$, Cho et al. reported the experimental results suggesting the transition between the vortex and FFLO states [38].

1.3 Organic superconductors $(\mathrm{TMTSF})_2X$

The organic compounds $(\mathrm{TMTSF})_2X$, which have a Q1D structure as mentioned in the following subsection, are clean type-II superconductors [39, 40]. Therefore, the FFLO state can occur in these compounds.

In $(\mathrm{TMTSF})_2\mathrm{ClO}_4$, Yonezawa et al. pointed out that the observed change of the principal axis in $T_{\mathrm{c}}^{\mathrm{onset}}(\phi)$ at a high field H_0 relates to the emergence of the FFLO state [14, 15]. Besides, they observed the up-turn at low temperatures in $H_{\mathrm{c}}(T)$, at which the value of $H_{\mathrm{c}}(T)$ exceeds the Pauli paramagnetic limit H_{P}. Lee et al. also observed a similar behavior of $H_{\mathrm{c}}(T)$ in $(\mathrm{TMTSF})_2\mathrm{PF}_6$ [41–43]. These behaviors are similar to that in the FFLO state where the Fermi surfaces touch on a line. In addition, Yonezawa et al. showed that the superconducting state at high fields is weak for impurity scattering. This result also coincides with the scenario that the FFLO state occurs [15].

1.3.1 Crystal structure

In this subsection, we review the crystal structure of $(\mathrm{TMTSF})_2X$, which is crucial for a close comparison between theoretical and experimental results.

The Q1D superconductor $(\mathrm{TMTSF})_2\mathrm{ClO}_4$ has a crystal structure as shown in Fig. 1.5 [39, 44, 45]. TMTSF molecules are stacked in the a-axial direction. Overlap of π-orbits of TMTSF molecules is largest in the a-axial direction. In the c-axial direction, the electron transfer is blocked by anion layers. Hence, $t_a > t_b \gg t_c$, where t_a, t_b, and t_c denote the hopping integrals in a-, b-, and c-axial directions, respectively.

Pévelen et al. obtained the cell parameters, which are $a = 7.083$ Å, $b = 15.334$ Å, $c = 13.182$ Å, $\alpha = 84.40°$, $\beta = 87.62°$, and $\gamma = 69.00°$ at low temperatures and under atmospheric pressure from their X-ray crystallography [45, 46]. We use these parameters, except for a value of b. For the following reason, we have halved the value of b as $b = 7.667$ Å.

In $(\mathrm{TMTSF})_2\mathrm{ClO}_4$, anions order in b-axial direction at low temperatures under ambient pressure. Because of the anion order, the unit cell doubles in this direction, and the Brillouin zone is halved. The anion order affects the energy dispersion near the edges of the halved Brillouin zone. However, it is expected that this change in the energy dispersion is negligible for the FFLO state, as shown in the later section, because the position of k_y on the Fermi surfaces touched by the vector $\boldsymbol{q}$ of the FFLO state is far away from the band edges. Also in a simplified model, $\boldsymbol{q} \parallel \boldsymbol{a}$, and the touching of the Fermi surfaces is far away from the band edges [47].

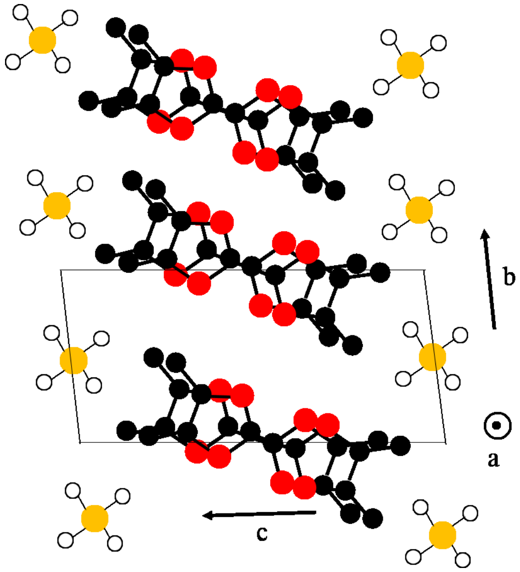

Figure 1.5: View of crystal structure of $(\mathrm{TMTSF})_2\mathrm{ClO}_4$ along a-axis.

1.3.2 Previous studies on the superconductivity in Q1D systems

In this subsection, we review previous studies for the anisotropic superconductivity and the FFLO state in Q1D systems.

The pairing symmetry in the (TMTSF)$_2X$ and its origin have been examined by many authors. Hasegawa and Fukuyama showed theoretical curves of NMR relaxation time for singlet and triplet states [48], and obtained a qualitative agreement between the experimental data in (TMTSF)$_2$ClO$_4$ by Takigawa et al. [49] and theoretical curve for these states with line node at the Fermi surfaces. This singlet state with line node is called the d-wave state. The detailed NMR measurement by Shinagawa et al. indicated the d-wave state [50]. Yonezawa et al. suggested that the gap structure of a superconducting state in (TMTSF)$_2$ClO$_4$ has line node, from the field-angle dependence of the heat capacity [51, 52]. Shimahara showed that the d-wave component in the pairing interaction mediated by antiferromagnetic fluctuations is attractive and maximum [18].

Although the d-wave pairing is most likely pairing symmetry in (TMTSF)$_2$ClO$_4$, other pairing symmetries have been discussed. Belin and Beniha suggested a superconducting state with a nodeless gap, from the temperature dependence of the thermal conductivity in (TMTSF)$_2$ClO$_4$ [53]. Oh et al. obtained the phase diagram determined by the temperature dependence of magnetic torque in (TMTSF)$_2$ClO$_4$, and showed that $H_{\mathrm{c2}} > H_{\mathrm{P}}$ at low temperature. They discussed the possibility of a spin-triplet superconducting state [55]. Also in a similar compound (TMTSF)$_2$PF$_6$, the spin susceptibility via NMR Knight shift measurement indicated a spin-triplet superconducting state [54]. Suginishi and Shimahara showed that the spin-triplet superconductivity with a nodeless gap can be induced by phonons in Q1D systems, which coincides with the above experimental results [17]. Tanaka and Kuroki et al.

studied the gap anisotropy due to the pairing interaction mediated by charge and spin fluctuations, and examined the f-wave pairing superconducting state induced by such a pairing interaction [56–60].

Pairing symmetries can be different in $(\mathrm{TMTSF})_2\mathrm{ClO}_4$ and $(\mathrm{TMTSF})_2\mathrm{PF}_6$, but the origin of pairing interaction can be similar, because crystal structure and electronic states in these compounds are similar. It has been shown that singlet and triplet attractive channels coexist in the pairing interaction mediated by antiferromagnetic fluctuations [19]. Fukui and Kato examined the mixing state where the odd- and even-frequency superconducting states coexist [61].

The FFLO state in $(\mathrm{TMTSF})_2X$ has been theoretically studied by many authors [62–67]. Lebed and Wu compared their theoretical curve of $H_{\mathrm{c2}}(T)$ with the experimental data by Yonezawa et al. [14], and obtained a good overall qualitative and quantitative agreement [68]. Croutoru, Houzet, and Buzdin studies interplay between the orbital effect and the FFLO modulation [69, 70]. Croutoru and Buzdin also examined the FFLO state on layered superconductors in a parallel magnetic field, and showed the resonance between the FFLO modulation and the Josephson coupling [71–73]. Miyazaki et al. obtained the magnetic field dependence of the transition temperature considered higher-order terms in the b-axial direction of the energy dispersion [74]. Miyawaki and Shimahara examined the effect of the Fermi surface anisotropy in Q1D systems, and found a dimensional crossover induced by the temperature [21], in which the behavior of the upper critical field continuously changes from that in 1D system at high temperatures to that in 2D system at low temperatures via a small shoulder between them. Aizawa et al. examined the FFLO state where singlet and triplet pairing symmetries coexist because of the pairing interaction mediated by charge fluctuations [75, 76].

1.4 Purpose of the thesis

As mentioned in Section 1.3, although various theoretical studies for the FFLO state in Q1D systems have been done (see § 1.3.2), the direction of the principal axis of $T_\mathrm{c}^\mathrm{onset}(\phi)$ observed in (TMTSF)$_2$ClO$_4$ at $H = H_0$ has not been reproduced. In this thesis, we theoretically try to reproduce this direction.

The observed change of the principal axis, if caused by a transition to the FFLO state, must primarily originate from the emergence of the nonzero FFLO vector $\boldsymbol{q}$. Unless the orbital pair-breaking effect is extremely weak, the FFLO modulation can occur in the direction parallel to the magnetic field. In (TMTSF)$_2$ClO$_4$, $H_\mathrm{c}(T) \propto T_\mathrm{c}^{(0)} - T$ near $H = 0$, which indicates that the orbital pair-breaking effect is not negligibly small. Therefore, it is reasonable to assume that $\boldsymbol{q} \parallel \boldsymbol{H}$ [10, 16].

Even when $\boldsymbol{q} = 0$, the transition temperature $T_\mathrm{c}(\phi)$ and the upper critical temperature $h_\mathrm{c}(\phi)$ depend on ϕ because of the orbital pair-breaking effect, and they reflect the anisotropy of the Fermi surface. In (TMTSF)$_2X$, the hopping integral on the a-axis is much larger than the others. Therefore, the orbital pair-breaking effect must be predominantly determined by the magnitude of $\boldsymbol{H}$'s component perpendicular to the intra-chain, which is consistent with the observed behavior of $T_\mathrm{c}^\mathrm{onset}(\phi)$ below H_0. Therefore, below H_0, the anisotropy of $T_\mathrm{c}^\mathrm{onset}(\phi)$ primarily originates from the orbital pair-breaking effect, and the Pauli paramagnetic pair-breaking effect does not significantly contribute to the anisotropy. In contrast, in the FFLO state, the nesting effect due to the finite $\boldsymbol{q}$ causes the anisotropy of $T_\mathrm{c}(\phi)$ and $h_\mathrm{c}(\phi)$. Because $\boldsymbol{q} \parallel \boldsymbol{H}$ owing to the weak orbital pair-breaking effect, the anisotropy of $T_\mathrm{c}(\phi)$ depends on the in-plane magnetic field direction. When $\boldsymbol{q} \neq 0$, $\phi_{\boldsymbol{q}} = \phi$, where $\phi_{\boldsymbol{q}}$ denotes the angle between $\boldsymbol{q}$ and the crystal a-axis.

On the basis of this purpose and background, we examine the in-plane-magnetic-field-direction dependence of the stability of the FFLO state in Q1D systems. To focus on the nesting effect, we assume that the orbital pair-breaking effect is sufficiently strong to lock the direction of $\boldsymbol{q}$ along $\boldsymbol{H}$, but is negligible in the equations for $T_{\rm c}$ and $H_{\rm c}$. The latter part of this assumption is not quantitatively justified for (TMTSF)$_2$ClO$_4$; however, even in our simplified model, it would be possible to clarify the direction of the magnetic fields that most stabilize the FFLO state.

Since we are motivated by above experimental results in (TMTSF)$_2$ClO$_4$, we show realistic parameter sets to reproduce the experimental results. However, our study is not limited to these compounds, and we examine with a wide range of parameters in Q1D systems.

In addition, in the Q1D compounds (TMTSF)$_2X$, as mentioned in § 1.3.2, various pairing symmetries have been discussed by many authors. In the FFLO state, the order-parameter mixing effect can occur because of the nonzero FFLO vector $\boldsymbol{q}$ and Zeeman energy. Therefore, the mixing effect can occur in (TMTSF)$_2X$. From the experimental $H_{\rm c}(T)$ in (TMTSF)$_2X$, it might be expected that the tricritical temperature T^* is larger than $0.56T_{\rm c}^{(0)}$. The mixing effect can enhance T^*. In addition, this effect also affects the optimum direction of $T_{\rm c}^{\rm onset}(\phi)$ because the anisotropy of the mixed order parameter affects the nesting effect. Therefore, in addition to the nesting effect, we examine the FFLO state in the presence of the mixing effect.

Chapter 2

Superconductivity in the magnetic field

In this chapter, we review the superconductivity in the magnetic field. The superconductors are classified into type-I and type-Ⅱ superconductors for $\kappa < 1/\sqrt{2}$ and $\kappa > 1/\sqrt{2}$, respectively. Here, $\kappa = \lambda/\xi$ denotes the Ginzburg-Landau (GL) parameter, where λ and ξ are the London's magnetic-field penetration depth and the coherence length, respectively.

2.1 Type-I superconductors

In type-I superconductors, in which $\kappa < 1/\sqrt{2}$, since the surface energy is positive, the magnetic field does not penetrate into superconductors, and the perfect diamagnetic state occurs inside superconductors.

When the magnetic field increases, the perfect diamagnetic state becomes unstable at the thermodynamic critical field H_{c}. H_{c} is derived from the condition $F_{\mathrm{s}}(T, H_{\mathrm{c}}(T)) = F_{\mathrm{n}}(T, H_{\mathrm{c}}(T))$, where F_{s} and F_{n} are the free energy for the BCS and normal states, respectively. From $F(T, H) = -T \log \mathrm{Tr}[\mathrm{e}^{-\beta\mathcal{H}}]$, F_s and F_n are expressed by

$$\begin{aligned} F_\mathrm{s} = &-\frac{2}{\beta}\sum_{\boldsymbol{k}}\Bigg[\log\left(1+\mathrm{e}^{-\beta E_\sigma(\boldsymbol{k})}\right) + \xi(\boldsymbol{k}) - E(\boldsymbol{k}) \\ &+ \Delta_0^2(\boldsymbol{k})\frac{1 - f(E_\downarrow(\boldsymbol{k})) - f(E_\uparrow(\boldsymbol{k}))}{2E(\boldsymbol{k})}\Bigg], \end{aligned} \tag{2.1}$$

$$F_\mathrm{n} = -\frac{2}{\beta}\sum_{\boldsymbol{k}}\Bigg[\log\left(1+\mathrm{e}^{-\beta\xi_\sigma(\boldsymbol{k})}\right) + \xi(\boldsymbol{k}) - |\xi(\boldsymbol{k})|\Bigg], \tag{2.2}$$

in the weak coupling limit. Here, $E_\sigma(\boldsymbol{k}) = E(\boldsymbol{k}) - \sigma h$, $E(\boldsymbol{k}) = \sqrt{\xi^2(\boldsymbol{k}) + \Delta_0^2(\boldsymbol{k})}$, $\xi_\sigma(\boldsymbol{k}) = \xi(\boldsymbol{k}) - \sigma h$, $\xi(\boldsymbol{k}) = \epsilon(\boldsymbol{k}) - \mu$, $h \equiv \mu_\mathrm{e}|\boldsymbol{H}|$, and $f(x) = 1/(\mathrm{e}^{\beta x} + 1)$. μ denotes the chemical potential.

From Eqs. (2.1) and (2.2), $F_\mathrm{n}(T, H) - F_\mathrm{n}(T, 0) = -H^2/8\pi$ and $F_\mathrm{s}(0, 0) - F_\mathrm{n}(0, 0) = -N(0)\Delta_0^2/2$, where the right-hand side is called the condensation energy of the superconductivity. Since in type-I superconductors $H = 0$ except for the region near the surface, $F_\mathrm{s}(0, H) = F_\mathrm{s}(0, 0)$. Therefore, since $F_\mathrm{s}(0, H_\mathrm{c}) = F_\mathrm{n}(0, H_\mathrm{c})$,

$$\frac{H_\mathrm{c}^2}{8\pi} = \frac{1}{2}N(0)\Delta_0^2. \tag{2.3}$$

Because $\epsilon_\mathrm{F} \approx 1/N(0) \gg \Delta \approx k_\mathrm{B}T$, H_c is significantly small. For example, the critical field is approximately 0.01 T for type-I superconductor Al.

2.2 Type-II superconductors

In type-II superconductors, when the magnetic field H increases, the magnetic field penetrates at $H > H_{\mathrm{c1}}$, where H_{c1} is the lower critical field. When the magnetic field increases further, the superconducting state is broken at the upper critical field H_{c2}, which is determined by both spin and orbital pair-breaking effects. The spin pair-breaking effect, which is called the Pauli paramagnetic pair-breaking effect, is caused by the Zeeman energy $\boldsymbol{H} \cdot \boldsymbol{S}$. The orbital pair-breaking effect is caused by the orbital motion of electrons. In the classical mechanics, the orbital motion of the charged particle is taken into account by the Lorentz force $e\boldsymbol{v} \times \boldsymbol{H}$. In the quantum mechanics, that is taken into account by the replacement of $\boldsymbol{p}$ with $\boldsymbol{p} + e\boldsymbol{A}/c$, where $\boldsymbol{A}$ denotes the vector potential.

2.2.1 Orbital limit H_{c20}

At $H_{\mathrm{c1}} < H < H_{\mathrm{c2}}$, the penetrating magnetic fields are quantized with the unit of $\Phi_0 = h/2e$, and the vortex is formed by the orbital motion of the charged particles. On the central axis of the quantum flux, the superconductivity is locally broken, while the superconductivity is restored at the position ξ away from this axis. These quantum fluxes form the triangle vortex lattice, and the superconducting state is stable, which is called the vortex state.

The magnitude of the orbital pair-breaking effect is characterized by H_{c20}, which is the upper critical field in the absence of the spin pair-breaking effect [77]. Approximate expression

$$H_{\mathrm{c20}} \approx \Delta_0^2 \frac{c}{e\hbar v_{\mathrm{F}}^2} \tag{2.4}$$

is obtained by considering the Lorentz force and the coherence length.

2.2.2 Pauli paramagnetic limit H_{P}

As mentioned in the previous chapter, the Pauli paramagnetic limit H_{P} is the magnetic field at which the superconducting condensation energy coincides with the spin polarization energy $\chi H^2/2$ in the absence of the orbital pair-breaking effect, where χ is the spin susceptibility [20]. At $H = H_{\mathrm{P}}$, the superconducting state is broken. In this subsection, we review the Pauli paramagnetic limit [8, 11, 23].

When we take into account the anisotropy of the gap function at $T = 0$, H_{P} is determined by

$$\frac{N_\alpha(0)|\Delta_\alpha^{(0)}|^2}{2} = \frac{\chi {H_{\mathrm{P}}}^2}{2}, \tag{2.5}$$

where $N_\alpha(0)$ and $\Delta_\alpha^{(0)}$ are the density of state at the Fermi energy and the energy gap of the symmetry index α, respectively. Here, $\Delta_\alpha^{(0)} = \Delta_{\alpha 0}/\bar{\gamma_\alpha}$, where $\Delta_{\alpha 0} = 2\hbar\omega_{\mathrm{D}} \exp\left(-1/g_\alpha N_\alpha(0)\right)$ and

$$\frac{1}{\bar{\gamma_\alpha}} = \exp\left[\frac{\langle[\gamma_\alpha(\boldsymbol{k})]^2 \log\left(1/|\gamma_\alpha(\boldsymbol{k})|\right)\rangle_{\mathrm{F}}}{\langle[\gamma_\alpha(\boldsymbol{k})]^2\rangle_{\mathrm{F}}}\right]. \tag{2.6}$$

$\gamma_\alpha(\boldsymbol{k})$ is the basis function of symmetry index α. We have defined the average over the Fermi surface as

$$\langle\cdots\rangle_{\mathrm{F}} = \sum_{s=\pm}\int_{-\pi}^{\pi}\frac{\mathrm{d}k_y}{2\pi}\frac{\rho(0,k_y,s)}{N(0)}(\cdots), \tag{2.7}$$

where $\rho(0, k_y, s)$ is the density of state at the Fermi energy with $s = \mathrm{sgn}(k_x)$. Thus, the Pauli paramagnetic limit in α-wave state at $T = 0$ is

$$\frac{\mu_{\mathrm{e}} H_{\mathrm{P}}}{\Delta_{\alpha 0}} = \frac{\sqrt{\langle[\gamma_\alpha(\boldsymbol{k})]^2\rangle_{\mathrm{F}}}}{\bar{\gamma_\alpha}}\frac{1}{\sqrt{2}}. \tag{2.8}$$

For the s-wave state, $\mu_{\mathrm{e}} H_{\mathrm{P}}/\Delta_{\mathrm{s}0} = 1/\sqrt{2}$.

At finite temperatures, the difference ΔF between F_{s} and F_{n} is

$$\begin{aligned}\Delta F = T\sum_{\boldsymbol{k},\sigma}\log\left(\frac{1+\mathrm{e}^{\beta(|\xi(\boldsymbol{k})|+\sigma h)}}{1+\mathrm{e}^{\beta(E(\boldsymbol{k})+\sigma h)}}\right)\\ +\sum_{\boldsymbol{k}}\left[|\xi(\boldsymbol{k})|-E(\boldsymbol{k})+\Delta_0^2(\boldsymbol{k})\frac{1-f(E_\downarrow(\boldsymbol{k}))-f(E_\uparrow(\boldsymbol{k}))}{2E(\boldsymbol{k})}\right],\end{aligned} \tag{2.9}$$

where $\Delta_0(\boldsymbol{k})=\Delta_0(T)\gamma_\alpha(\boldsymbol{k})$. When $\Delta F=0$,

$$\begin{aligned}\frac{1}{2}\left(\frac{\Delta_0(T)}{\Delta_\alpha^{(0)}}\right)^2\left(1+2\log\left|\frac{\Delta_\alpha^{(0)}}{\Delta_0(T)}\right|\right) = 2\frac{T}{\Delta_\alpha^{(0)}}\frac{\Delta_0(T)}{\Delta_\alpha^{(0)}}\sum_{s=\pm}\int_{-\pi}^{\pi}\frac{\mathrm{d}k_y}{2\pi}\frac{\rho(0,k_y,s)}{N_\alpha(0)}\gamma_\alpha(\boldsymbol{k})\\ \times\sum_\sigma\int_0^\infty \mathrm{d}p\ \cosh p\ \log\left(\frac{1+\mathrm{e}^{-\beta(|\Delta_0(\boldsymbol{k})\sinh p|+\sigma h)}}{1+\mathrm{e}^{-\beta(|\Delta_0(\boldsymbol{k})\cosh p|+\sigma h)}}\right).\end{aligned} \tag{2.10}$$

On the other hand, the gap equation in the magnetic field is expressed as

$$\Delta(\boldsymbol{k})=\frac{1}{N}\sum_{\boldsymbol{k}'}V(\boldsymbol{k},\boldsymbol{k}')\frac{1-f(E_\downarrow(\boldsymbol{k}'))-f(E_\uparrow(\boldsymbol{k}'))}{2E(\boldsymbol{k}')}\Delta(\boldsymbol{k}'), \tag{2.11}$$

where $V(\boldsymbol{k},\boldsymbol{k}')$ is the pairing interaction. In the weak coupling limit, the gap equation is rewritten as

$$\log\frac{\Delta_\alpha^{(0)}}{\Delta_0(T)}=\sum_{s=\pm}\int_{-\pi}^{\pi}\frac{\mathrm{d}k_y}{2\pi}\frac{\rho(0,k_y,s)[\gamma_\alpha(\boldsymbol{k})]^2}{N_\alpha(0)}\sum_\sigma\int_0^\infty \mathrm{d}p\log\left(\frac{1}{1+\mathrm{e}^{\beta(\Delta_0(\boldsymbol{k})\cosh p+\sigma h)}}\right). \tag{2.12}$$

We solve Eqs. (2.10) and (2.12) simultaneously, and obtain the first-order transition point (h_{P},T) between the BCS and normal states.

2.2.3 The FFLO state

The ratio of the strength of Pauli paramagnetic and orbital pair-breaking effects is expressed by the Maki parameter [78]

$$\alpha=\frac{\sqrt{2}H_{\mathrm{c20}}}{H_{\mathrm{P}}}. \tag{2.13}$$

As mentioned in Section 1.2, for the FFLO state to occur, it is required that $H_{c20} \gtrsim H_{\mathrm{P}}$. In conventional type-II superconductors, the orbital pair-breaking effect is strong ($\alpha \ll 1$). However, in exotic superconductors, such as heavy fermion and organic superconductors, it can be that $\alpha > 1$ because of the heavy effective mass and narrow band width. For example, it has been shown that $\alpha \approx 8$ for κ-(BEDT-TTF)Cu(NCS)$_2$ [29] and $\alpha = 3.94$ for β"-(BEDT-TTF)SF$_5$CH$_2$CF$_2$SO$_3$ [38]. Therefore, the FFLO state can occur in these superconductors.

In this subsection, we review the FFLO state in the presence of a weak orbital pair-breaking effect, and survey many studies [79–87] as a reference.

Gruenberg and Gunther examined the FFLO state in the presence of the orbital pair-breaking effect in isotropic 3D systems [16]. They showed that the FFLO state coexists with the vortex state when $\alpha > 1.8$, and that the direction of the FFLO vector $\boldsymbol{q}$ is locked in that of the magnetic field $\boldsymbol{H}$ in this case: $\boldsymbol{q} \parallel \boldsymbol{H}$. In other words, when the orbital pair-breaking effect is sufficiently weak, the FFLO modulation can occur in the direction parallel to the vortex line. If the orbital pair-breaking effect is ignored; i.e., when $\alpha = \infty$, the direction of the magnetic field is locked in the optimum direction that is determined from the Fermi surface.

Shimahara and Rainer examined the relation between the vortex and FFLO states in isotropic 2D systems, and showed that the pure FFLO state coincides with the vortex state in the limit $n_{\mathrm{L}} \to \infty$, where n_{L} is Landau level index, as reviewed below [10].

When the magnetic field is applied to the y-z plane; $\boldsymbol{H} = H(0, \cos\theta, \sin\theta)$, the magnitude of the orbital pair-breaking effect is expressed by $\kappa_\perp = 2cH\sin\theta/e$, which vanishes in the limit $\theta \to 0$. In this limit, the relational equation between the FFLO and vortex states is

$$q = \lim_{\kappa_\perp \to 0} \sqrt{2 n_{\rm L} \kappa_\perp}. \tag{2.14}$$

For the FFLO vector q to be finite in the limit $\kappa_\perp \to 0$, the Landau level index $n_{\rm L}$ diverges such as $n_{\rm L} \approx 1/\kappa_\perp$.

We define $\eta^\dagger = (\mathbf{\Pi}_x + i\mathbf{\Pi}_y)$, where $\mathbf{\Pi} = -i\hbar\nabla - 2e\boldsymbol{A}/c$, which satisfies

$$\eta^\dagger \phi_{n_{\rm L}} = \sqrt{n_{\rm L}} e^{i\varphi_0} \phi_{n_{\rm L}}, \tag{2.15}$$

for the eigenfunction $\phi_{n_{\rm L}}$ of infinitely large $n_{\rm L}$, where φ_0 is the angle between the momentum $\boldsymbol{q}$ and k_x-axis in the momentum space. The eigenfunction is expressed as

$$\phi_{n_{\rm L}} = \frac{1}{\sqrt{n_{\rm L}!}} (\eta^\dagger)^{n_{\rm L}} \phi_0, \tag{2.16}$$

where

$$\phi_0 = \mathrm{e}^{ikx} \exp\left[-\frac{\kappa_\perp}{2}(y - \frac{k}{\kappa_\perp})^2 \right] \tag{2.17}$$

is the Abrikosov function, and k is a parameter. The solution of Eq. (2.15) is $\phi_{n_{\rm L}} \propto \exp(i\boldsymbol{q}\cdot\boldsymbol{r})$, where $\boldsymbol{q} = (q\cos\varphi_0, q\sin\varphi_0, 0)$ and $q = \lim_{\kappa_\perp \to 0} \sqrt{2n_{\rm L}\kappa_\perp}$.

Therefore, in the limit $\kappa_\perp \to 0$, the Abrikosov function can have large Landau level indices $n_{\rm L}$. The order parameters with $n_{\rm L} \gg 1$ exhibit a spatial modulation perpendicular to the vortex line. This modulation is physically equivalent to the FFLO modulation because in the limit $n_{\rm L} \to \infty$, the vortex state is reduced to the FFLO state. To sum up, when the orbital pair-breaking effect is sufficiently weak, the Landau level index diverges, and the FFLO modulation occurs in the direction parallel to $\boldsymbol{H}$.

Chapter 3

Anisotropic superconductivity in Q1D systems

Mechanisms of the anisotropic superconductivity have been examined by many authors. As mentioned in Chapter 1, because the anisotropic superconductivity contributes to the FFLO state, in the thesis, we examine the FFLO state on various pairing symmetries. In this chapter, we survey pairing interactions mediated by phonons and antiferromagnetic fluctuations in Q1D systems, which induce the anisotropic superconductivity. Our assumption for the pairing symmetry is based on the survey in this chapter.

3.1 Triplet superconductivity induced by phonons

The attractive interaction mediated by phonons can cause the superconductivity. In Q1D organic superconductors (TMTSF)$_2X$, from the observation of the isotope effect [88], it has been suggested that the pairing interaction mediated by phonons can contribute to the superconductivity. Although the pairing interaction mediated by phonons usually causes the singlet superconductivity with full-gap, it also can cause triplet superconductivity. In this section, we review that the triplet superconductivity can be induced by phonons [17, 89].

The electron-phonon Hamiltonian is

$$H_{\mathrm{e-ph}} = \sum_{\boldsymbol{k},\boldsymbol{q}} \sum_{\sigma,\sigma'} M(\boldsymbol{q})(b_{\boldsymbol{q}} + b^{\dagger}_{-\boldsymbol{q}}) c^{\dagger}_{\boldsymbol{k}\sigma} c_{\boldsymbol{k}-\boldsymbol{q}\sigma'}, \tag{3.1}$$

where $c^{\dagger}_{\boldsymbol{k}\sigma}$ ($c_{\boldsymbol{k}\sigma}$) and $b^{\dagger}_{\boldsymbol{q}}$ ($b_{\boldsymbol{q}}$) are creation (annihilation) operators of electrons with $\boldsymbol{k}\sigma$ and phonons with $\boldsymbol{q}$, respectively. $M(\boldsymbol{q})$ is the electron-phonon coupling constant. In the following, we ignore the momentum dependence of $M(\boldsymbol{q})$ as $M(\boldsymbol{q}) \equiv g$. In the weak coupling limit, the effective interaction between electrons mediated by phonons is

$$V_{\mathrm{eff}}(\boldsymbol{k} - \boldsymbol{k}') = -g \frac{q_{\mathrm{s}}^2}{|\boldsymbol{k} - \boldsymbol{k}'|^2 + q_{\mathrm{s}}^2}, \tag{3.2}$$

for $|\xi(\boldsymbol{k})|$, $|\xi(\boldsymbol{k}')| < \omega_{\mathrm{D}}$, where q_{s} and ω_{D} are the inverse screening length and the Debye frequency, respectively. This interaction has been studied by many authors [90–93]. Suginishi and Shimahara examined this pairing interaction, taking into account the correction of short-range and long-range parts of Coulomb interactions, and showed phase diagrams [17].

The gap equation is expressed as

$$\Delta(\boldsymbol{k}) = -\frac{1}{N} \sum_{\boldsymbol{k}'} V(\boldsymbol{k} - \boldsymbol{k}') \frac{\tanh\left(E(\boldsymbol{k}')/2T\right)}{2E(\boldsymbol{k}')} \Delta(\boldsymbol{k}'). \tag{3.3}$$

The Q1D dispersion is defined by $\epsilon(\boldsymbol{k}) = -2t_a \cos{(k_x a_{\mathrm{s}})} - 2t_b \cos{(k_y b_{\mathrm{s}})}$, where a_{s} and b_{s} are lattice constants along a- and b-axial directions, respectively. When $t_a \gg t_b$, there exist the Fermi surfaces $\pm k_x^{\mathrm{F}}(k_y)$ in the first Brillouin zone.

The pairing interaction at the Fermi surfaces can be written as

$$V(\boldsymbol{k}-\boldsymbol{k}') = V(k_x^{\mathrm{F}}(k_y) \pm k_x^{\mathrm{F}}(k'_y), k_y - k'_y) \equiv V^{(+\pm)}(k_y, k'_y). \tag{3.4}$$

We define $\tilde{V}^{(+\pm)}(k_y, k'_y) = \sqrt{\rho(k_y)}V^{(+\pm)}(k_y, k'_y)\sqrt{\rho(k'_y)}$, where $\sqrt{\rho(k_y)} = 1/[4\pi t_a \sin(k_x^{\mathrm{F}}(k_y)a_{\mathrm{s}})]$. $\tilde{V}^{(+\pm)}(k_y, k'_y)$ can be expanded as

$$\tilde{V}^{(+\pm)}(k_y, k'_y) = \sum_{n,m}[V_{nm}^{(+\pm)}\gamma_n(k_y)\gamma_m(k'_y) + \bar{V}_{nm}^{(+\pm)}\bar{\gamma}_n(k_y)\bar{\gamma}_m(k'_y)], \tag{3.5}$$

with expansion factors $V_{nm}^{(+\pm)}$ and $\bar{V}_{nm}^{(+\pm)}$ and basis functions $\gamma_m(k_y)$ and $\bar{\gamma}_m(k_y)$, where $\gamma_m(k_y) = n_m \cos(mk_y b_{\mathrm{s}})$ and $\bar{\gamma}_m(k_y) = n_m \sin(mk_y b_{\mathrm{s}})$ with normalization factors $n_m = \sqrt{2}$ for $m \neq 0$ and $n_m = 1$ for $m = 0$. The pairing symmetry is classified by an integer m and the symmetry of the order parameter with respect to the inversion of k_x. For example, for $\gamma_0(k_y) = 1$ and $\Delta(k_x, k_y) = \Delta(-k_x, k_y)$, the s-wave state is defined. For $\gamma_0(k_y) = 1$ and $\Delta(k_x, k_y) = -\Delta(-k_x, k_y)$, the $\mathrm{p_x}$-wave state is defined.

It has been shown that the $\mathrm{p_x}$-wave state is favorable in Q1D superconductors if the s-wave state is suppressed by weak screening and strong on-site Coulomb repulsive interaction [17]. This condition is satisfied for realistic parameters in $(\mathrm{TMTSF})_2X$. This theoretical result coincides with the experimental results of NMR Knight shift and the thermal conductivity in $(\mathrm{TMTSF})_2\mathrm{PF}_6$ [53, 54]. Therefore, we examine the FFLO state, taking into account the contribution of the triplet pairing.

3.2 Pairing interaction mediated by antiferromagnetic fluctuations

In Q1D superconductors (TMTSF)$_2X$, because the superconducting phase appears in proximately to the antiferromagnetic phase in the phase diagram in the pHT space [25]. The pairing interaction mediated by antiferromagnetic fluctuations has been examined by many authors [18, 94–96]. In this section, we review the anisotropic superconductivity induced by this pairing interaction [18].

3.2.1 d-wave pairing

In this subsection, we review that the d-wave superconductivity can be induced by antiferromagnetic fluctuations.

This theory is carried out by using the Hubbard model

$$\mathcal{H} = \sum_{\boldsymbol{k}\sigma} \epsilon(\boldsymbol{k}) c^\dagger_{\boldsymbol{k}\sigma} c_{\boldsymbol{k}\sigma} + U \sum_{\boldsymbol{k},\boldsymbol{k}',\boldsymbol{q}} c^\dagger_{\boldsymbol{k}+\boldsymbol{q}\uparrow} c_{\boldsymbol{k}\uparrow} c^\dagger_{\boldsymbol{k}'-\boldsymbol{q}\downarrow} c_{\boldsymbol{k}'\downarrow}, \tag{3.6}$$

where U is the on-site Coulomb.

In the random-phase-approximation (RPA), the spin- and charge-susceptibilities are obtained as

$$\chi_{\mathrm{s}}(\boldsymbol{q}) = \frac{\chi_0(\boldsymbol{q})}{1 - U\chi_0(\boldsymbol{q})} \tag{3.7}$$

and

$$\chi_{\mathrm{c}}(\boldsymbol{q}) = \frac{\chi_0(\boldsymbol{q})}{1 + U\chi_0(\boldsymbol{q})}, \tag{3.8}$$

respectively, where

$$\chi_0(\boldsymbol{q}) = \frac{1}{N} \sum_{\boldsymbol{k}} \frac{f(\epsilon(\boldsymbol{k})) - f(\epsilon(\boldsymbol{k}+\boldsymbol{q}))}{\epsilon(\boldsymbol{k}+\boldsymbol{q}) - \epsilon(\boldsymbol{k})} \tag{3.9}$$

is the static free susceptibility. In the same approximation, the effective pairing interaction between electrons is obtained as

$$\Gamma_{\uparrow\downarrow}(\boldsymbol{k},\boldsymbol{k}') = \ \gamma_1(\boldsymbol{k}-\boldsymbol{k}') + \gamma_2(\boldsymbol{k}+\boldsymbol{k}'), \tag{3.10}$$

where

$$\begin{aligned} \gamma_1(\boldsymbol{k}-\boldsymbol{k}') &= U - \frac{1}{2}\frac{U^2\chi_0(\boldsymbol{k}-\boldsymbol{k}')}{1+U\chi_0(\boldsymbol{k}-\boldsymbol{k}')} + \frac{1}{2}\frac{U^2\chi_0(\boldsymbol{k}-\boldsymbol{k}')}{1-U\chi_0(\boldsymbol{k}-\boldsymbol{k}')}, \\ \gamma_2(\boldsymbol{k}+\boldsymbol{k}') &= \frac{1}{2}\frac{U^2\chi_0(\boldsymbol{k}+\boldsymbol{k}')}{1-U\chi_0(\boldsymbol{k}+\boldsymbol{k}')}. \end{aligned} \tag{3.11}$$

The singlet and triplet pairing interactions between electrons on the sites separating by the relative coordinate vector (m, n) are expressed as

$$\begin{aligned} V_{nm}^{\mathrm{sin}} &= \frac{1}{N}\sum_{\boldsymbol{q}}(\gamma_1(\boldsymbol{q}) + \gamma_2(\boldsymbol{q}))\mathrm{e}^{imq_x+inq_y}, \\ V_{nm}^{\mathrm{tri}} &= \frac{1}{N}\sum_{\boldsymbol{q}}(\gamma_1(\boldsymbol{q}) - \gamma_2(\boldsymbol{q}))\mathrm{e}^{imq_x+inq_y}. \end{aligned} \tag{3.12}$$

For realistic parameter $t_b = 0.15t_a$ and $U \approx 1.48t$ in (TMTSF)$_2X$, it has been shown that V_{nm}^{sin} is attractive and maximum for $n = 0$ and $m = 2$, which means that the gap function $\sqrt{2}\Delta_{20}\cos(2k_x)$ can appear in Q1D systems. The pairing symmetry with this gap function is called the d-wave pairing symmetry, which has line nodes at the Fermi surfaces. Therefore, we examine the d-wave FFLO state in Q1D systems.

3.2.2 Coexistence of singlet and triplet attractive channels

In this subsection, we review that the pairing interaction mediated by antiferromagnetic fluctuations includes both singlet and triplet pairing attractive channels [19].

Let us consider the pairing interaction mediated by spin fluctuations expressed by

$$H' = -g\sum_{i,j}\chi_{ij}\boldsymbol{S}_i\cdot\boldsymbol{S}_j, \tag{3.13}$$

where g is the coupling constant, i and j are lattice sites, and χ_{ij} is the expression of the spin susceptibility in the real space. Equation (3.13) is rewritten as

$$\begin{aligned} H' = &-\frac{g}{N}\sum_{\boldsymbol{k},\boldsymbol{k}'}\chi(\boldsymbol{k}-\boldsymbol{k}')\Big[-\frac{3}{4}\psi^\dagger_{00}(\boldsymbol{k})\psi_{00}(\boldsymbol{k}') \\ &+\frac{1}{4}(\psi^\dagger_{11}(\boldsymbol{k})\psi_{11}(\boldsymbol{k}')+\psi^\dagger_{1-1}(\boldsymbol{k})\psi_{1-1}(\boldsymbol{k}')+\psi^\dagger_{10}(\boldsymbol{k})\psi_{10}(\boldsymbol{k}'))\Big], \end{aligned} \tag{3.14}$$

where $\psi_{11}(\boldsymbol{k}) = c_{-\boldsymbol{k}\uparrow}c_{\boldsymbol{k}\uparrow}$, $\psi_{1-1}(\boldsymbol{k}) = c_{-\boldsymbol{k}\downarrow}c_{\boldsymbol{k}\downarrow}$, $\psi_{10}(\boldsymbol{k}) = (c_{-\boldsymbol{k}\uparrow}c_{\boldsymbol{k}\downarrow}+c_{-\boldsymbol{k}\downarrow}c_{\boldsymbol{k}\uparrow})/\sqrt{2}$, and $\psi_{00}(\boldsymbol{k}) = (c_{-\boldsymbol{k}\uparrow}c_{\boldsymbol{k}\downarrow}-c_{-\boldsymbol{k}\downarrow}c_{\boldsymbol{k}\uparrow})/\sqrt{2}$.

For antiferromagnetic correlations, $\chi_{ij} < 0$ and $\chi_{ij} > 0$ on the same and different sublattices, respectively. In a square lattice tight-binding model near the half-filling, $\chi_{ij} \equiv \bar{\chi}_1 < 0$ and $\chi_{ij} \equiv \bar{\chi}_2 > 0$ for the nearest-neighbor and next-nearest-neighbor sites, respectively. It is verified from Eq. (3.14) that the former favors the singlet pairing, while the latter favors the triplet pairing.

The gap equation by this pairing interaction is

$$\begin{pmatrix} \Delta_1 \\ \Delta_2 \end{pmatrix} = -V \begin{pmatrix} \bar{\chi}_1 W_{11} & \bar{\chi}_1 W_{12} \\ \bar{\chi}_2 W_{21} & \bar{\chi}_2 W_{22} \end{pmatrix} \begin{pmatrix} \Delta_1 \\ \Delta_2 \end{pmatrix}, \tag{3.15}$$

where the matrix elements W_{nm} are

$$W_{nm} = \frac{1}{N}\sum_{\boldsymbol{k}}\gamma_n(\boldsymbol{k})\gamma_m(\boldsymbol{k})\frac{\tanh\left(\epsilon(\boldsymbol{k})/2T\right)}{2\epsilon(\boldsymbol{k})}. \tag{3.16}$$

The eigenvalue of the matrix in the right-hand-side of Eq. (3.15) is

$$\lambda = \frac{1}{2}\left[(\bar{\chi}_1 W_{11}+\bar{\chi}_2 W_{22}) \pm \sqrt{(\bar{\chi}_1 W_{11}+\bar{\chi}_2 W_{22})^2 - 4\bar{\chi}_1\bar{\chi}_2(W_{11}W_{22}-W_{12}^2)}\right]. \tag{3.17}$$

Since $\bar{\chi}_1\bar{\chi}_2 < 0$ and $W_{11}W_{22} - W_{12}^2 > 0$, the second term in Eq. (3.17) is positive. Therefore, two eigenvalues have opposite signs, which implies that both singlet and triplet pairing interactions are attractive channels.

It has been shown that in the Q1D Hubbard model as reviewed in the previous subsection, $V_{10}^{\rm tri} < 0$ and $V_{40}^{\rm tri} < 0$ for realistic parameters within the RPA. These interactions induce the gap functions $\Delta_{10} \sin k_x$ and $\Delta_{40} \sin 4k_x$, respectively, the symmetries of which are called p-wave and f-wave pairing symmetries, respectively. Hence, the pairing interaction mediated by antiferromagnetic fluctuations contains both singlet and triplet pairing attractive channels. In this case, the singlet and triplet order parameters coexist. Therefore, we need to examine the FFLO state in the presence of the mixing effect.

Chapter 4

Theory of the FFLO state

As mentioned in the purpose, we do not consider the orbital pair-breaking effect, except for $\boldsymbol{q} \parallel \boldsymbol{H}$. Thus, Hamiltonian is represented by

$$\mathcal{H} = \sum_{\boldsymbol{k},\sigma} \xi_\sigma(\boldsymbol{k}) c^\dagger_{\boldsymbol{k}\sigma} c_{\boldsymbol{k}\sigma} - \frac{1}{N} \sum_{\boldsymbol{k},\boldsymbol{k}'\boldsymbol{q}} V(\boldsymbol{k},\boldsymbol{k}',\boldsymbol{q}) c^\dagger_{\boldsymbol{k}+\boldsymbol{q}\uparrow} c^\dagger_{-\boldsymbol{k}\downarrow} c_{-\boldsymbol{k}'\downarrow} c_{\boldsymbol{k}'+\boldsymbol{q}\uparrow}, \tag{4.1}$$

where $V(\boldsymbol{k},\boldsymbol{k}',\boldsymbol{q})$ is the pairing interaction.

It is supposed that there exists three-dimensionality to stabilize the superconducting long-range order and to justify the mean-field approximation, but we ignore k_z for simplicity. We apply the mean-field approximation to Eq. (4.1):

$$\mathcal{H}_{\mathrm{MF}} = \sum_{\boldsymbol{k},\sigma} \xi_\sigma(\boldsymbol{k}) c^\dagger_{\boldsymbol{k}\sigma} c_{\boldsymbol{k}\sigma} + \sum_{\boldsymbol{k}} \Delta^*_{\boldsymbol{q}} c_{-\boldsymbol{k}+\frac{\boldsymbol{q}}{2}\downarrow} c_{\boldsymbol{k}+\frac{\boldsymbol{q}}{2}\uparrow} + \sum_{\boldsymbol{k}} \Delta_{\boldsymbol{q}} c^\dagger_{\boldsymbol{k}+\frac{\boldsymbol{q}}{2}\uparrow} c^\dagger_{-\boldsymbol{k}+\frac{\boldsymbol{q}}{2}\downarrow}, \tag{4.2}$$

where

$$\Delta_{\boldsymbol{q}}(\boldsymbol{k}) = -\frac{1}{N} \sum_{\boldsymbol{k}'} V(\boldsymbol{k},\boldsymbol{k}') \langle c_{-\boldsymbol{k}'+\frac{\boldsymbol{q}}{2}\downarrow} c_{\boldsymbol{k}'+\frac{\boldsymbol{q}}{2}\uparrow} \rangle, \tag{4.3}$$

which is the order parameter in the FFLO state.

We assume

$$V(\boldsymbol{k},\boldsymbol{k}') = -g_\alpha \gamma_\alpha(\boldsymbol{k}) \gamma_\alpha(\boldsymbol{k}'), \tag{4.4}$$

where g_α and $\gamma_\alpha(\boldsymbol{k})$ are coupling constants and basis functions of the symmetry index α, respectively. Thus,

$$\Delta_{\boldsymbol{q}}(\boldsymbol{k}) = \ \Delta_\alpha \gamma_\alpha(\boldsymbol{k}). \tag{4.5}$$

We express basis functions of the singlet pairing as

$$\gamma_{\mathrm{s}}(k_y) = 1 \quad , \quad \gamma_{\mathrm{d}}(k_y) = \sqrt{2}\cos k_y. \tag{4.6}$$

for s- and d-wave states, respectively. We express basis functions of the triplet pairing as

$$\gamma_{\mathrm{p_x}}(s, k_y) = \ s \quad , \quad \gamma_{\mathrm{p_y}}(k_y) = \ \sqrt{2}\sin k_y \tag{4.7}$$

and

$$\gamma_{\mathrm{f_x}}(s, k_y) = \ \sqrt{2} s \cos k_y \quad , \quad \gamma_{\mathrm{f_y}}(k_y) = \ \sqrt{2}\sin 2k_y \tag{4.8}$$

for p- and f-wave states, respectively.

The momentum dependence of these states may appear to originate from the inter-chain pairing. For example, in the d-wave state, the momentum dependence is expressed as $\gamma_{\mathrm{d}} \propto \cos(2k_x)$ as mentioned in § 3.2.1. The momentum dependence of $\gamma_{\mathrm{d}} \propto \cos k_y$ simulates the structure of the gap function of the d-wave state near the Fermi surface.

We do not consider the mixing with the parallel spin pairing states in the triplet pairing for the following reasons. Firstly, transitions to the parallel spin pairing states have not been observed in experimental. Secondly, such interactions in these states are much smaller than the antiparallel spin pairing interactions [35].

4.1 Spatial modulation of the order parameter

In this section, we mention the FFLO modulation. The order parameter spatially oscillates because of the nonzero FFLO vector $\boldsymbol{q}$ [3, 97]. The order parameter of the FFLO state is expressed by

$$\Delta^{\dagger}_{\boldsymbol{q}}(\boldsymbol{k}) = \langle c^{\dagger}_{-\boldsymbol{k}+\frac{1}{2}\boldsymbol{q}\downarrow} c^{\dagger}_{\boldsymbol{k}+\frac{1}{2}\boldsymbol{q}\uparrow} \rangle, \tag{4.9}$$

where $\boldsymbol{q}$ and $\boldsymbol{k}$ are center-of-mass and relative momenta, respectively. In the coordinate representation, the order parameter is expressed by

$$\Delta^{*}(\boldsymbol{r}, \boldsymbol{r}') = \langle \psi^{\dagger}_{\uparrow}(\boldsymbol{r}) \psi^{\dagger}_{\downarrow}(\boldsymbol{r}') \rangle. \tag{4.10}$$

Here, we define the center-of-mass and relative coordinates as $\boldsymbol{R}$ and $\boldsymbol{\rho}$, respectively. Equation (4.10) is rewritten as

$$\begin{aligned} \Delta^{*}(\boldsymbol{R}, \boldsymbol{\rho}) &= \frac{1}{N} \sum_{\boldsymbol{k}_1, \boldsymbol{k}_2} \mathrm{e}^{-i(\boldsymbol{k}_1+\boldsymbol{k}_2)\cdot\boldsymbol{R}} \mathrm{e}^{-i(\boldsymbol{k}_1-\boldsymbol{k}_2)\cdot\boldsymbol{\rho}} \langle c^{\dagger}_{\boldsymbol{k}_1\uparrow} c^{\dagger}_{\boldsymbol{k}_2\downarrow} \rangle \\ &= \frac{1}{N} \sum_{\boldsymbol{k}, \boldsymbol{q}} \mathrm{e}^{-i\boldsymbol{q}\cdot\boldsymbol{R}} \mathrm{e}^{-i\boldsymbol{k}\cdot\boldsymbol{\rho}} \langle c^{\dagger}_{\boldsymbol{k}+\frac{1}{2}\boldsymbol{q}\uparrow} c^{\dagger}_{-\boldsymbol{k}+\frac{1}{2}\boldsymbol{q}\downarrow} \rangle. \end{aligned} \tag{4.11}$$

By using Fourier transformation,

$$\Delta^{*}(\boldsymbol{R}, \boldsymbol{k}) = \sum_{\boldsymbol{q}} \mathrm{e}^{-i\boldsymbol{q}\cdot\boldsymbol{R}} \Delta^{\dagger}_{\boldsymbol{q}}(\boldsymbol{k}). \tag{4.12}$$

Thus, the order parameter spatially oscillates because of the FFLO vector $\boldsymbol{q}$.

In general, there exist several equivalent $\boldsymbol{q}$, and these $\boldsymbol{q}$ provide the same upper critical field at the second-order transition point. Therefore, the order parameter is

$$\Delta(\boldsymbol{R}) = \sum_{m=1}^{M} \Delta_m \mathrm{e}^{i\boldsymbol{q}_m\cdot\boldsymbol{R}}, \tag{4.13}$$

where M is the number of degenerate $\boldsymbol{q}$. In the isotropic symmetry, $M = \infty$. If we require a periodicity of the order parameter in the real space, M can take 1, 2, 3, 4, or 6. When $M = 1$, the order parameter is expressed as

$$\Delta(\boldsymbol{R}) = \mathrm{e}^{i\boldsymbol{q}\cdot\boldsymbol{R}}\Delta_1, \tag{4.14}$$

the state of which was examined by Fulde and Ferrell [4]. Larkin and Ovchinnikov examined the state for $M = 2$ in 3D isotropic systems [5]. In this state, the order parameter is expressed as

$$\Delta(\boldsymbol{R}) = \Delta_1 \cos(\boldsymbol{q}\cdot\boldsymbol{R}). \tag{4.15}$$

It has been shown that the free energy of Eq. (4.15) is lower than that of Eq. (4.14). In the states of $M = 3$, $M = 4$, and $M = 6$, because nodes of the order parameter in the real space increase at the second-order transition point, a gain of the spin polarization energy increases. Thus, it has been shown that free energy in these states is lower than that in states of Eqs. (4.14) and (4.15) at low temperatures and high magnetic fields [97].

The number of degenerate $\boldsymbol{q}$ is determined by the symmetry of the Fermi surface or the gap function. When we consider the Q1D system where the Fermi surfaces are symmetric with respect to the k_x- and k_y-axes, it is expected that $M = 4$ at the second-order transition point. When $\boldsymbol{q}$ is parallel to the k_x- or k_y-axes in the above system, it is expected that $M = 2$. Also, when the Q1D Fermi surfaces are not symmetric with respect to the k_x- and k_y-axes, and are symmetric with respect to the origin, it is expected that $\boldsymbol{q}$ and $-\boldsymbol{q}$ are degenerate at the second-order transition point. This is why the FFLO state can have $\boldsymbol{q}$ and $-\boldsymbol{q}$ or more than $\boldsymbol{q}$ values. However, we examined the second-order transition point where a single $\boldsymbol{q}$ is assumed.

4.2 Formulation at finite temperatures

In this section, we derive the formulation at finite temperatures. We diagonalize Eq. (4.2) by a Bogoliubov transformation

$$c_{\boldsymbol{k}+\frac{\boldsymbol{q}}{2}\uparrow} = u_{\boldsymbol{k}}\alpha_{\boldsymbol{k}\uparrow} + v_{\boldsymbol{k}}\alpha^{\dagger}_{-\boldsymbol{k}\downarrow} \quad , \quad c_{-\boldsymbol{k}+\frac{\boldsymbol{q}}{2}\downarrow} = u_{\boldsymbol{k}}\alpha_{-\boldsymbol{k}\downarrow} - v_{\boldsymbol{k}}\alpha^{\dagger}_{\boldsymbol{k}\uparrow}. \tag{4.16}$$

Thus, the gap equation is obtained as

$$\Delta_{\boldsymbol{q}}(\boldsymbol{k}) = \frac{1}{N}\sum_{\boldsymbol{k}'} V(\boldsymbol{k},\boldsymbol{k}')\frac{1 - f(E_{\boldsymbol{k}'\uparrow}) - f(E_{\boldsymbol{k}'\downarrow})}{2E_{\boldsymbol{k}'}}\Delta_{\boldsymbol{q}}(\boldsymbol{k}'), \tag{4.17}$$

where $E_{\boldsymbol{k}\sigma} = E_{\boldsymbol{k}} + \sigma\zeta$, and $E_{\boldsymbol{k}} = \sqrt{\xi^2(\boldsymbol{k}) + \Delta^2_{\boldsymbol{q}}(\boldsymbol{k})}$. In Q1D systems, because one of the hopping integrals is much larger than the others, the Fermi surfaces are open at the edges of the first Brillouin zone, and there exist the Fermi surfaces $\pm k_x^{\rm F}(k_y)$ in the first Brillouin zone. We define

$$\zeta = h_{\rm c}\left(\frac{\boldsymbol{v}_{\rm F}(s,k_y)\cdot\boldsymbol{q}}{2h_{\rm c}} - 1\right), \tag{4.18}$$

where $\boldsymbol{v}_{\rm F}(s,k_y)$ is the Fermi velocity, and $s = {\rm sgn}(k_x)$.

Taking the limit of $\Delta_{\boldsymbol{q}} \to 0$ in the gap equation Eq. (4.17), we obtain the equation of the second-order transition point $(h_{\rm c}(\boldsymbol{q}), T_{\rm c}(\boldsymbol{q}))$ between the FFLO and normal states,

$$\begin{aligned}\log\frac{T_{\rm c}}{T^{(0)}_{{\rm c}\alpha}} &= \int_0^\infty {\rm d}y \sum_{s=\pm}\int_{-\pi}^{\pi}\frac{{\rm d}k_y}{2\pi}\frac{\rho_\alpha(0,s,k_y)}{N_\alpha(0)} \\ &\quad\times \sinh^2\frac{\beta\zeta}{2}\frac{\tanh y}{y\,(\cosh^2 y + \sinh^2(\beta\zeta/2))}.\end{aligned} \tag{4.19}$$

For numerical calculation, we rewrite Eq. (4.19) as

$$\begin{aligned}\log\frac{T_{\rm c}}{T^{(0)}_{{\rm c}\alpha}} &= -\sum_{s=\pm}\int_{-\pi}^{\pi}\frac{{\rm d}k_y}{2\pi}\frac{\rho_{\alpha\alpha}(0,s,k_y)}{N_\alpha(0)}\sinh^2(\frac{\beta\zeta}{2})\int_0^\infty {\rm d}y\log y \\ &\quad\times\left[\frac{2\sinh^2 y}{(\cosh^2 y + \sinh^2(\beta\zeta/2))^2} - \frac{1}{\cosh^2 y(\cosh^2 y + \sinh^2(\beta\zeta/2))}\right],\end{aligned} \tag{4.20}$$

where

$$\rho_{\alpha\alpha}(0,s,k_y) = \rho(0,s,k_y)[\gamma_\alpha(s,k_y)]^2, \tag{4.21}$$

and

$$N_\alpha(0) = \sum_{s=\pm}\int_{-\pi}^{\pi}\frac{\mathrm{d}k_y}{2\pi}\rho_{\alpha\alpha}(0,s,k_y). \tag{4.22}$$

Here, $\rho(\xi,s,k_y)$ is the density of state defined by

$$\frac{1}{N}\sum_{\boldsymbol{k}} F(\boldsymbol{k}) = \sum_{s=\pm}\int \mathrm{d}\xi \int_{-\pi}^{\pi}\frac{\mathrm{d}k_y}{2\pi}\rho(\xi,s,k_y)F(\boldsymbol{k}), \tag{4.23}$$

for the arbitrary smooth function $F(\xi,s,k_y) = F(\boldsymbol{k})$.

4.3 Formulation at $T = 0$

Next, we derive the formulation at $T = 0$. We define the normal and anomalous Green functions by

$$\begin{aligned} G(t-t') =& -i\langle T[c_{\boldsymbol{k}'\uparrow}(t)c^\dagger_{\boldsymbol{k}\uparrow}(t')]\rangle, \\ F^\dagger(t-t') =& \, i\langle T[c^\dagger_{-\boldsymbol{k}\downarrow}(t)c^\dagger_{\boldsymbol{k}+\boldsymbol{q}\uparrow}(t')]\rangle, \end{aligned} \tag{4.24}$$

respectively, where $T[\cdots]$ and $\langle A\rangle$ represent time-ordered product and quantum mechanical expectation of physical quantity A, respectively. The equations of motion of the Green functions are

$$\begin{aligned} i\frac{\partial}{\partial t}G(t-t') &= \delta(t-t')\delta_{\boldsymbol{k},\boldsymbol{k}'} - i\langle T[[c_{\boldsymbol{k}\uparrow}(t),\mathcal{H}_{\mathrm{MF}}]c^\dagger_{\boldsymbol{k}\uparrow}(t')]\rangle, \\ i\frac{\partial}{\partial t}F^\dagger(t-t') &= i\langle T[c^\dagger_{-\boldsymbol{k}\downarrow}(t)[c^\dagger_{\boldsymbol{k}+\boldsymbol{q}\uparrow}(t'),\mathcal{H}_{\mathrm{MF}}]]\rangle. \end{aligned} \tag{4.25}$$

We obtain $F^\dagger(\boldsymbol{k},\omega)$ and $G(\boldsymbol{k},\omega)$ by Fourier transformation:

$$\begin{aligned} (\omega + i\delta\omega - \xi(\boldsymbol{k}) + h)G(\boldsymbol{k},\omega) + \Delta_{\boldsymbol{q}}(\boldsymbol{k})F^\dagger(\boldsymbol{k},\omega) &= 1, \\ (\omega + i\delta\omega + \xi(\boldsymbol{k}+\boldsymbol{q}) + h)F^\dagger(\boldsymbol{k},\omega) + \Delta^*_{\boldsymbol{q}}(\boldsymbol{k})G(\boldsymbol{k},\omega) &= 0. \end{aligned} \tag{4.26}$$

Thus, we obtain the gap equation at $T = 0$

$$\begin{aligned} \Delta_{\boldsymbol{q}}(\boldsymbol{k}) = & -\frac{1}{N}\sum_{\boldsymbol{k}'} V(\boldsymbol{k},\boldsymbol{k}') \\ & \times \int_{-\infty}^{\infty}\frac{\mathrm{d}\omega}{2\pi i}\frac{\Delta^*_{\boldsymbol{q}}(\boldsymbol{k})}{(\omega + i\delta\omega - \xi(\boldsymbol{k}) + h)(\omega + i\delta\omega + \xi(\boldsymbol{k}+\boldsymbol{q}) + h) + |\Delta_{\boldsymbol{q}}(\boldsymbol{k})|^2}. \end{aligned} \tag{4.27}$$

Taking limit $\Delta_q \to 0$ in the gap equation Eq. (4.27), we obtain

$$\frac{h_{\mathrm{c}}}{\Delta_{\alpha 0}} = \frac{1}{2}\exp\left[-\sum_{s=\pm}\int_{-\pi}^{\pi}\frac{\mathrm{d}k_y}{2\pi}\frac{\rho_{\alpha\alpha}(0,k_y,s)}{N_\alpha}\log\left|1 - \frac{\boldsymbol{v}_{\mathrm{F}}(s,k_y)\cdot\boldsymbol{q}}{2h_{\mathrm{c}}}\right|\right]. \tag{4.28}$$

Equation (4.28) coincides with Eq. (4.20) in the limit $T \to 0$.

4.4 Order-parameter mixing effect

As mentioned in § 3.2.2, in Q1D organic superconductors (TMTSF)$_2X$, it is expected that singlet and triplet attractive channels coexist in the pairing interaction. In addition, in the FFLO state, the order parameters of the singlet and triplet pairing are mixed. Thus, the pairing interaction can be expanded as

$$V(\boldsymbol{k},\boldsymbol{k}') = -\sum_{\alpha} g_\alpha \gamma_\alpha(\boldsymbol{k})\gamma_\alpha(\boldsymbol{k}'), \tag{4.29}$$

as a result,

$$\Delta_{\boldsymbol{q}}(\boldsymbol{k}) = \sum_{\alpha} \Delta_\alpha \gamma_\alpha(\boldsymbol{k}). \tag{4.30}$$

By solving the gap equation Eq. (4.17) using Eqs. (4.29) and (4.30), we obtain the equation where the order-parameter mixing effect is taken into account at finite temperatures:

$$\begin{pmatrix} \Delta_{\alpha_1} \\ \Delta_{\alpha_2} \end{pmatrix} \log \frac{T_{\rm c}}{T^{(0)}_{{\rm c}\alpha_1}} = -\begin{pmatrix} M_{\alpha_1\alpha_1} & M_{\alpha_1\alpha_2} \\ M_{\alpha_2\alpha_1} & M_{\alpha_2\alpha_2} - G_{\alpha_1\alpha_2} \end{pmatrix} \begin{pmatrix} \Delta_{\alpha_1} \\ \Delta_{\alpha_2} \end{pmatrix}, \tag{4.31}$$

where

$$\begin{aligned} M_{\alpha_1\alpha_2} = & \sum_{s=\pm} \int_{-\pi}^{\pi} \frac{{\rm d}k_y}{2\pi} \frac{\rho_{\alpha_1\alpha_2}(0,s,k_y)}{N_{\alpha_1}(0)} \sinh^2 (\frac{\beta\zeta}{2}) \int_0^\infty {\rm d}y \log y \\ & \times \left[\frac{2\sinh^2 y}{(\cosh^2 y + \sinh^2(\beta\zeta/2))^2} - \frac{1}{\cosh^2 y(\cosh^2 y + \sinh^2(\beta\zeta/2))} \right], \end{aligned} \tag{4.32}$$

and

$$G_{\alpha_1\alpha_2} = \log \frac{T^{(0)}_{{\rm c}\alpha_2}}{T^{(0)}_{{\rm c}\alpha_1}} = \frac{1}{g_{\alpha_2}N_{\alpha_2}(0)} - \frac{1}{g_{\alpha_1}N_{\alpha_1}(0)}. \tag{4.33}$$

From Eq. (4.31), we obtain $T_{\rm c} = {\rm e}^{-\lambda(\boldsymbol{q},h_{\rm c},T_{\rm c})} T^{(0)}_{{\rm c}\alpha_1}$, where λ is the smallest eigenvalue of the matrix of the right-hand-side in Eq. (4.31).

At $T = 0$, we obtain

$$\begin{pmatrix} \Delta_{\alpha_1} \\ \Delta_{\alpha_2} \end{pmatrix} \log \frac{2h_{\rm c}}{\Delta_{\alpha_1 0}} = \begin{pmatrix} M_{\alpha_1\alpha_1} & M_{\alpha_1\alpha_2} \\ M_{\alpha_2\alpha_1} & M_{\alpha_2\alpha_2} - G_{\alpha_1\alpha_2} \end{pmatrix} \begin{pmatrix} \Delta_{\alpha_1} \\ \Delta_{\alpha_2} \end{pmatrix}, \tag{4.34}$$

where $M_{\alpha_1\alpha_2}$ is the formula at $T = 0$:

$$M_{\alpha_1\alpha_2} = \sum_{s=\pm} \int_{-\pi}^{\pi} \frac{\mathrm{d}k_y}{2\pi} \frac{\rho_{\alpha_1\alpha_2}(0, k_y, s)}{N_{\alpha_1}} \log \left| 1 - \frac{\boldsymbol{v}_\mathrm{F}(s, k_y) \cdot \boldsymbol{q}}{2h_\mathrm{c}} \right|. \tag{4.35}$$

We obtain $h_\mathrm{c} = \mathrm{e}^{-\lambda(\boldsymbol{q}, h_\mathrm{c})} \Delta_{\alpha_1 0}$ from Eq. (4.34). The upper critical field $h_\mathrm{c}(\boldsymbol{q})$ and the transition temperature $T_\mathrm{c}(\boldsymbol{q})$ are given by optimizing the length $|\boldsymbol{q}|$.

We discuss the magnitude of the mixing effect in the Q1D dispersion $\epsilon(\boldsymbol{k}) = -2t_a \cos k_x - 2t_b \cos k_y$ when $\alpha_1 = \mathrm{s}, \mathrm{d}$ and $\alpha_2 = \mathrm{p}, \mathrm{f}$. As mentioned in § 1.2.2, the mixing effect enhances the tricritical point (h^*, T^*), which is defined by

$$\begin{aligned} h^*(\varphi_{\boldsymbol{q}}, t_b/t_a) &= \lim_{q \to 0} h_\mathrm{c}(q, \varphi_{\boldsymbol{q}}, t_b/t_a), \\ T^*(\varphi_{\boldsymbol{q}}, t_b/t_a) &= \lim_{q \to 0} T_\mathrm{c}(q, \varphi_{\boldsymbol{q}}, t_b/t_a). \end{aligned} \tag{4.36}$$

We suppose that the off-diagonal element $M_{\alpha_1\alpha_2}$ is proportional to $q^m (t_b/t_a)^l$ for small q and t_b/t_a with integers m and l. The mixing effect is strong as integers m and l decrease because $t_a \gg t_b$ in Q1D systems. We summarize m and l for each combination of α_1 and α_2, where $\varphi_{\boldsymbol{q}}$ is fixed, in Tab. 4.1 (for the derivation see Appendix B). Table 4.1 shows that $m = 1$ and $l = 0$ when $\alpha_1 = \mathrm{s}$ and $\alpha_2 = \mathrm{p_x}$, $\alpha_1 = \mathrm{d}$ and $\alpha_2 = \mathrm{f_x}$, and $\varphi_q = 0$, which means that the leading term in $M_{\alpha_1\alpha_2}$ is proportional to $q^1 (t_b/t_a)^0$. Therefore, the magnitude of the mixing effect is strong at $\varphi_{\boldsymbol{q}} = 0$. In contrast, when $\varphi_{\boldsymbol{q}} = \pi/2$, because $M_{\mathrm{sp_x}} = 0$ and $M_{\mathrm{df_x}} = 0$, the mixing effect does not occur. Table 4.1 shows that $m = 3$ and $l = 1$ when $\alpha_1 = \mathrm{d}$ and $\alpha_2 = \mathrm{p_x}$, which means that the leading term in $M_{\alpha_1\alpha_2}$ is proportional to $q^3 (t_b/t_a)^1$. Therefore, $M_{\mathrm{dp_x}} \ll 1$, and the magnitude of the mixing effect is weak. Table 4.1 shows that $m = 1$ and $l = 1$ when $\alpha_1 = \mathrm{s}$ and $\alpha_2 = \mathrm{p_y}$, $\alpha_1 = \mathrm{d}$ and $\alpha_2 = \mathrm{f_y}$, and $\varphi_{\boldsymbol{q}} = \pi/2$, while $M_{\mathrm{sp_y}} = 0$ and $M_{\mathrm{df_y}} = 0$ when $\varphi_{\boldsymbol{q}} = 0$. Therefore, the magnitude of the mixing effect is strong at $\varphi_{\boldsymbol{q}} = \pi/2$, while the mixing effect does not occur at $\varphi_{\boldsymbol{q}} = 0$.

Table 4.1: Integers m and l for each combination of α_1 and α_2 when $\varphi_{\boldsymbol{q}}$ is fixed. We show the results at $\varphi_{\boldsymbol{q}} = 0$ and $\varphi_{\boldsymbol{q}} = \pi/2$ for s-$\mathrm{p_x}$, d-$\mathrm{p_x}$, and d-$\mathrm{f_x}$ mixing states and s-$\mathrm{p_y}$, d-$\mathrm{p_y}$, and d-$\mathrm{f_y}$ mixing states, respectively. In the former states, $M_{\alpha_1\alpha_2} = 0$ at $\varphi_q = \pi/2$, while in the latter states, $M_{\alpha_1\alpha_2} = 0$ at $\varphi_q = 0$.

Combination	s-$\mathrm{p_x}$	d-$\mathrm{p_x}$	d-$\mathrm{f_x}$	s-$\mathrm{p_y}$	d-$\mathrm{p_y}$	d-$\mathrm{f_y}$
$\varphi_{\boldsymbol{q}}$	0			$\pi/2$		
m	1	3	1	1	1	1
l	0	1	0	1	2	1

Chapter 5

Application to organic superconductor $(\mathrm{TMTSF})_2\mathrm{ClO}_4$

We define the following energy dispersion as a model of the conduction electrons of $(\mathrm{TMTSF})_2\mathrm{ClO}_4$ [39, 44, 45, 98] by

$$\epsilon(\boldsymbol{k}) = \epsilon_{\mathrm{AA}}(\boldsymbol{k}) - \epsilon_{\mathrm{AB}}(\boldsymbol{k}), \tag{5.1}$$

where

$$\epsilon_{\mathrm{AA}}(\boldsymbol{k}) = -2t_{\mathrm{I3}} \cos k_y - 2t_{\mathrm{I4}} \cos (k_x - k_y), \tag{5.2}$$

$$\epsilon_{\mathrm{AB}}(\boldsymbol{k}) = \sqrt{\epsilon_0^2 + [\epsilon_1(\boldsymbol{k})]^2}, \tag{5.3}$$

$$\begin{aligned}[\epsilon_1(\boldsymbol{k})]^2 = {} & 2t_{\mathrm{S1}}t_{\mathrm{S2}} \cos k_x + 2(t_{\mathrm{S1}}t_{\mathrm{I1}} + t_{\mathrm{S2}}t_{\mathrm{I2}}) \cos k_y \\ & + 2(t_{\mathrm{S1}}t_{\mathrm{I2}} + t_{\mathrm{S2}}t_{\mathrm{I1}}) \cos (k_x - k_y) + 2t_{\mathrm{I1}}t_{\mathrm{I2}} \cos (k_x - 2k_y),\end{aligned} \tag{5.4}$$

and $\epsilon_0^2 = {t_{\mathrm{S1}}}^2 + {t_{\mathrm{S2}}}^2 + {t_{\mathrm{I1}}}^2 + {t_{\mathrm{I2}}}^2$. The hopping integrals t_{S1}, t_{S2}, t_{I1}, t_{I2}, t_{I3}, and t_{I4} are defined in Fig. 5.1. We express $\boldsymbol{k}$ as $\boldsymbol{k} = k_x\boldsymbol{a}^* + k_y\boldsymbol{b}^* + k_z\boldsymbol{c}^*$, where $\boldsymbol{a}^* = \boldsymbol{b} \times \boldsymbol{c}/[\boldsymbol{a} \cdot (\boldsymbol{b} \times \boldsymbol{c})]$, $\boldsymbol{b}^* = \boldsymbol{c} \times \boldsymbol{a}/[\boldsymbol{b} \cdot (\boldsymbol{c} \times \boldsymbol{a})]$, and $\boldsymbol{c}^* = \boldsymbol{a} \times \boldsymbol{b}/[\boldsymbol{c} \cdot (\boldsymbol{a} \times \boldsymbol{b})]$. Therefore, $k_x = \boldsymbol{k} \cdot \boldsymbol{a}$ and $k_y = \boldsymbol{k} \cdot \boldsymbol{b}$. For simplicity, we assume $k_z = 0$.

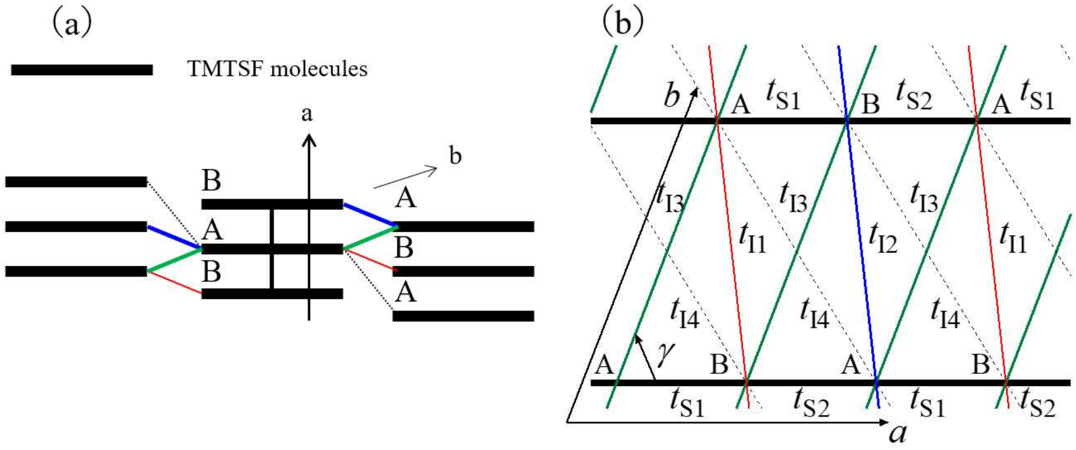

Figure 5.1: (a) Schematic figure of the structure of $(\mathrm{TMTSF})_2\mathrm{ClO}_4$. TMTSF molecules shown by black thick solid lines are dimerized, and the sites A and B are inequivalent. (b) Definition of the hopping integrals in real space. The unit cell contains two sites A and B. The black solid lines show t_{S1} and t_{S2}, respectively. The red solid, blue solid, green solid, and black dotted lines show t_{I1}, t_{I2}, t_{I3}, and t_{I4}, respectively. The angle γ and the lengths of the lines reflect the lattice parameter in $(\mathrm{TMTSF})_2\mathrm{ClO}_4$ obtained by Pévelen et al. described in § 1.3.1.

We summarize parameter sets in Tab. 5.1. The parameter sets $\mathrm{P_a}$ and $\mathrm{P_b}$ are based on X-ray crystallography [45]. Note that $\mathrm{A} \neq \mathrm{a}$ and $\mathrm{B} \neq \mathrm{b}$. We have defined A and B to distinguish TMTSF molecules due to the dimerization and a and b to distinguish parameter sets due to the influence of the anion order. The parameter set $\mathrm{A_{ave}}$ is obtained by the first-principles calculation [44]. Because we ignore the influence of the anion order, we use the parameter set $\mathrm{P_{ave}}$. The parameter sets $\mathrm{M_1}$ and $\mathrm{M_2}$ are obtained by modifying the inter-chain hopping integrals in the parameter set $\mathrm{P_{ave}}$, and reproduce the experimental results precisely.

Table 5.1: Parameter sets for $\mathrm{(TMTSF)_2ClO_4}$ in unit of meV. $\mathrm{P_a}$ and $\mathrm{P_b}$ are the parameter sets obtained by Pévelen et al. for the molecules that are nonequivalent as a result of the anion order. Because we ignore the influence of the anion order, we use $\mathrm{P_{ave}}$, which is parameter set obtained by averaging $\mathrm{P_a}$ and $\mathrm{P_b}$. $\mathrm{A_{ave}}$ is the parameter set by Alemany et al. at average structure 7K and 1kbar. $\mathrm{M_1}$ and $\mathrm{M_2}$ are parameter sets obtained by modifying $\mathrm{P_{ave}}$.

Parameter	$\mathrm{P_a}$	$\mathrm{P_b}$	$\mathrm{P_{ave}}$	$\mathrm{A_{ave}}$	$\mathrm{M_1}$	$\mathrm{M_2}$
t_{S1}	413	362	387.5	278.5	387.5	387.5
t_{S2}	324	335	329.5	242.6	329.5	329.5
t_{I1}	-50	-50	-50	-50.1	-50	-50
t_{I2}	-100	-100	-100	-56.4	-90	-90
$t_{\mathrm{I3}}(/t_{\mathrm{I5}})$	70(/71)	70(/71)	70.5	55.9	55	55
$t_{\mathrm{I4}}(/t_{\mathrm{I6}})$	20(/21)	20(/21)	20.5	-2.4	35	45

Figure 5.2 shows the Fermi surfaces derived for the parameter sets $\mathrm{A_{ave}}$, $\mathrm{P_{ave}}$, $\mathrm{M_1}$, and $\mathrm{M_2}$. We assume a half-filled hole band, which corresponds to a quarter-filled hole band in the absence of the dimerization of TMTSF molecules. The direction of the distortion of these Fermi surfaces is the same, although the magnitude of the distortion is different.

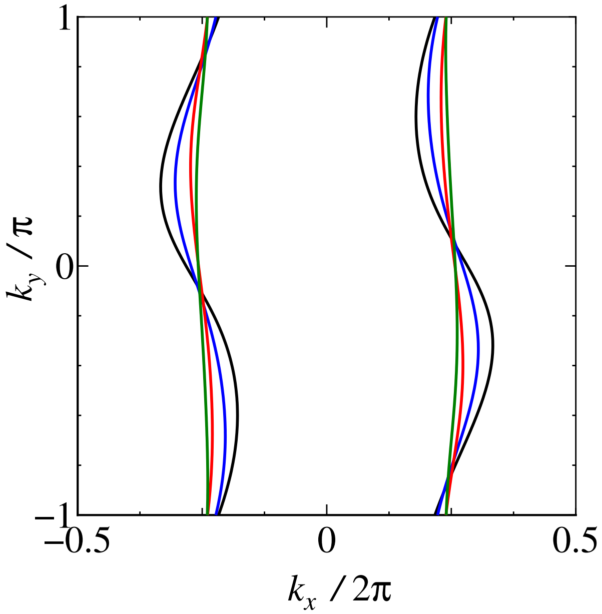

Figure 5.2: The black, blue, red, and green solid curves represent the Fermi surfaces for the parameter sets $\mathrm{A_{ave}}$, $\mathrm{P_{ave}}$,$\mathrm{M_1}$, and $\mathrm{M_2}$, respectively. Although $\boldsymbol{a}^*$ and $\boldsymbol{b}^*$ are not perpendicular to each other, k_x and k_y are drawn perpendicular to each other for the convenience.

In the FFLO state, the FFLO vector $\boldsymbol{q}$ is expressed as $\boldsymbol{q} = q_x \boldsymbol{a}^* + q_y \boldsymbol{b}^*$ (Fig. 5.3 (a)). For simplicity, we assume $q_z = 0$. $\boldsymbol{q}$ is expressed as

$$(q_x, q_y) = q_1(\cos\varphi_{\boldsymbol{q}}, \sin\varphi_{\boldsymbol{q}}), \tag{5.5}$$

where $\varphi_{\boldsymbol{q}}$ and q_1 are defined in Fig. 5.3 (b). Note that $q_1 \neq |\boldsymbol{q}| \equiv q$.

We define q_a and $q_{b'}$ by

$$(q_a, q_{b'}) \equiv (\boldsymbol{q}\cdot\hat{\boldsymbol{a}}, \boldsymbol{q}\cdot\hat{\boldsymbol{b}}') = q(\cos\phi_{\boldsymbol{q}}, \sin\phi_{\boldsymbol{q}}), \tag{5.6}$$

where $\phi_{\boldsymbol{q}}$ is shown in Fig. 5.3 (c). Here, we define the unit vector $\hat{\boldsymbol{b}}'$ that is perpendicular to $\hat{\boldsymbol{a}}$ and $\hat{\boldsymbol{b}}'\cdot\hat{\boldsymbol{b}} > 0$ by $\hat{\boldsymbol{b}}' = (\hat{\boldsymbol{b}} - \cos\gamma\hat{\boldsymbol{a}})/\sin\gamma$. Therefore,

$$q_a = \boldsymbol{q}\cdot\hat{\boldsymbol{a}} = \frac{1}{a}\boldsymbol{q}\cdot\boldsymbol{a} = \frac{1}{a}q_x, \tag{5.7}$$

$$q_{b'} = \boldsymbol{q}\cdot\hat{\boldsymbol{b}}' = (\frac{a}{b}\frac{q_y}{\sin\gamma} - \frac{q_x}{\tan\gamma})\frac{1}{a}, \tag{5.8}$$

and

$$\tan\phi_{\boldsymbol{q}} = \frac{1}{\sin\gamma}\frac{a}{b}\tan\varphi_{\boldsymbol{q}} - \frac{1}{\tan\gamma}. \tag{5.9}$$

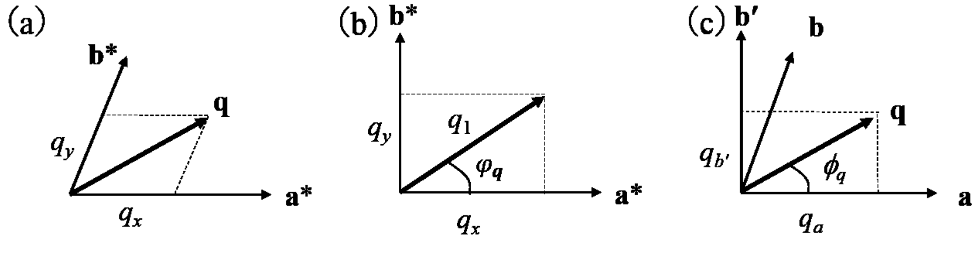

Figure 5.3: For the FFLO vector $\boldsymbol{q}$, we define (a) q_x and q_y, (b) $\varphi_{\boldsymbol{q}}$ and q_1, and (c) q_a, q'_b and $\phi_{\boldsymbol{q}}$. In the panel (b), $\boldsymbol{a}^*$ and $\boldsymbol{b}^*$ are drawn perpendicular to each other to define the angle $\varphi_{\boldsymbol{q}}$ and length q_1.

Chapter 6

Results : Stability of the FFLO state and phase diagrams

In this chapter, as mentioned in the purpose, the direction of $\boldsymbol{q}$ is locked in the direction of $\boldsymbol{H}$; i.e., $\phi_{\boldsymbol{q}} = \phi$, whereas the length $|\boldsymbol{q}|$ must be optimized so that h_{c} is maximized.

6.1 Dependence on the in-plane magnetic field direction

We examine the stability of the FFLO state depending on the in-plane magnetic field direction for both s- and d-wave states. We do not consider the mixing effect.

We numerically calculate Eq. (4.28) for parameter sets shown in Tab. 5.1. Figures 6.1 and 6.2 show the magnetic field angular dependence of the upper critical field for s- and d-wave states, respectively. Over wide ranges of ϕ, the upper critical fields $h_{\mathrm{c}}(\phi)$ are remarkably enhanced by the emergence of the FFLO state. In particular, they exhibit sharp cusps, at the tops of which $h_{\rm c}$ is more than six times the Pauli paramagnetic limit. For example, for the parameter set $\rm M_1$, the cusp occurs at $\phi \approx -0.3392\pi$. The maximum value is $h_{\rm c} \approx 3.925\Delta_{\rm d0}$, which is given by $q \approx 5.216 h_{\rm c}/t_{\rm S1}$. Their sharpness implies that the directions of the cusps must remain the optimum directions of the magnetic field that stabilize the FFLO state the most when the orbital pair-breaking effect is incorporated. The optimum directions are sensitive to changes in the inter-chain hopping integrals, whereas for all parameter sets, they are in the second and fourth quadrants, which do not contains the directions of $\pm\boldsymbol{b}$. This agrees with the observations in $T_{\rm c}^{\rm onset}(\phi)$. The parameter sets $\rm M_1$ and $\rm M_2$ give the maxima of $h_{\rm c}(\phi)$ near $\phi = -63.3^\circ$ and $\phi = -78.3^\circ$, at which the experimental $T_{\rm c}^{\rm onset}(\phi)$ have the maximum values when $H = 30$ kOe and $H = 47.5$ kOe [14], respectively.

At the cusps, it is easily verified that $n = 3$, which means that the terms in $\Delta k_x^{\rm F}(k_y, \boldsymbol{q})$ proportional to $(k_y - k_y^0)^1$ and $(k_y - k_y^0)^2$ vanish. This behavior is essentially the same as that in the square lattice system explained in § 1.2.1 [11], although the controlling parameters (ϕ and $n_{\rm h}$) are different.

Comparing Figs. 6.1 and 6.2, it is found that the optimum directions of ϕ do not strongly depend on the pairing symmetry for all parameter sets.

Figures 6.3 and 6.4 show $|\boldsymbol{q}|(\phi)$ for the parameter set $\rm M_1$ in s- and d-wave states, respectively. It is found that at each ϕ, the Fermi surfaces touch or nearly touch when $|\boldsymbol{q}|$ is optimized. At $\phi = -0.340\pi$, which is close to the optimum ϕ, the red closed circle shows that the optimum $|\boldsymbol{q}|$ makes the Fermi surfaces touch as shown in Fig. 6.5.

Comparing the blue closed triangles in the Figs. 6.3 and 6.4, which is the optimum $|\boldsymbol{q}|$ for $\phi \approx -0.199\pi$, it is found that the optimum $|\boldsymbol{q}|$ of the s-wave state is different from that of the d-wave state. In the s-wave state, the optimum $|\boldsymbol{q}|$ for $\phi \approx -0.199\pi$

makes the Fermi surfaces touch, and the optimum nesting point $k_y^0 \approx -0.6\pi$, as shown in Fig. 6.6. In contrast, in the d-wave state, the optimum $|\boldsymbol{q}|$ deviates from the red dashed curves, which means that the Fermi surfaces cross for the optimum $|\boldsymbol{q}|$ and the optimum nesting point $k_y^0 \approx 0.9\pi$ as shown in Fig. 6.7. These differences can be explained as follow. Although the amplitude of the order parameter in the d-wave state is small at the $k_y^0 \approx -0.6\pi$, where the Fermi surfaces touch, that is large at the $k_y^0 \approx 0.9\pi$, where the Fermi surfaces cross. Therefore, the Fermi surfaces nest so that the amplitude of the order parameter is large. Figure 6.8 shows the angluar dependence of the optimum nesting point and indicates the above explanation. In the regime of $-0.338 \lesssim \phi \lesssim 0.045\pi$ including the blue closed triangles, the optimum nesting point k_y^0 in the d-wave state, which is the light blue open circles in Fig. 6.8, has two points for an angle ϕ. This means that the Fermi surfaces cross, because the amplitude of the order parameter in the d-wave state is small at k_y^0 where the Fermi surfaces touch, as shown in the black open circles in Fig. 6.8.

Figure 6.5 also shows that the points at which the Fermi surfaces touch are far away from $k_y = \pi/2$, near which the anion order affects the electron dispersion. Hence, the anion order would not significantly change the present result.

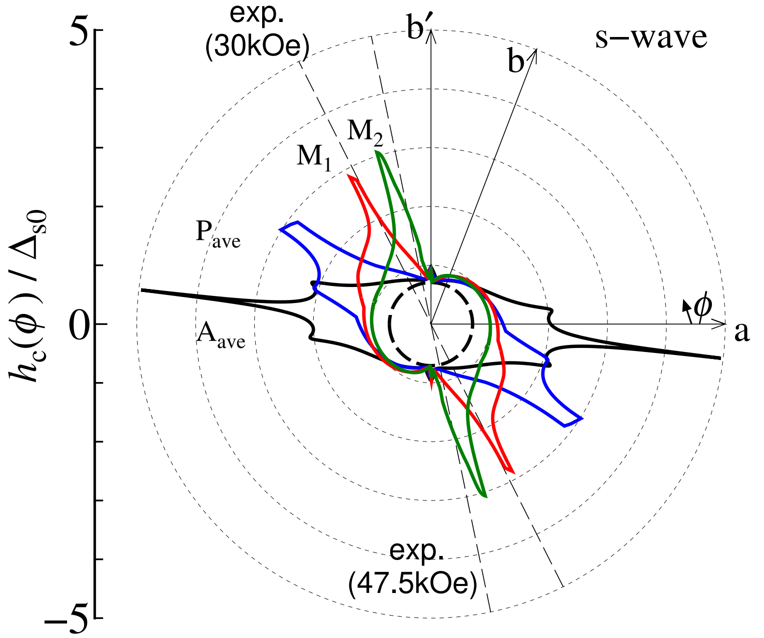

Figure 6.1: Magnetic field angular dependence of the upper critical field $h_c(\phi)$ for the s-wave state at $T = 0$ scaled by zero field gap Δ_{s0}. The black, blue, red, and green solid curves show the results for parameter sets A_{ave}, P_{ave}, M_1, and M_2, respectively. The bold dashed circle shows the Pauli paramagnetic limit $h_P/\Delta_{s0} = 1/\sqrt{2} \approx 0.7071$. The dashed straight lines represent directions of the magnetic field ($\phi = -63.3°$ and $\phi = -78.3°$) at which the experimental $T_c^{onset}(\phi)$ has a maximum value for $H = 30$ kOe and $H = 47.5$ kOe, respectively [14]. This figure is presented in Ref. [99].

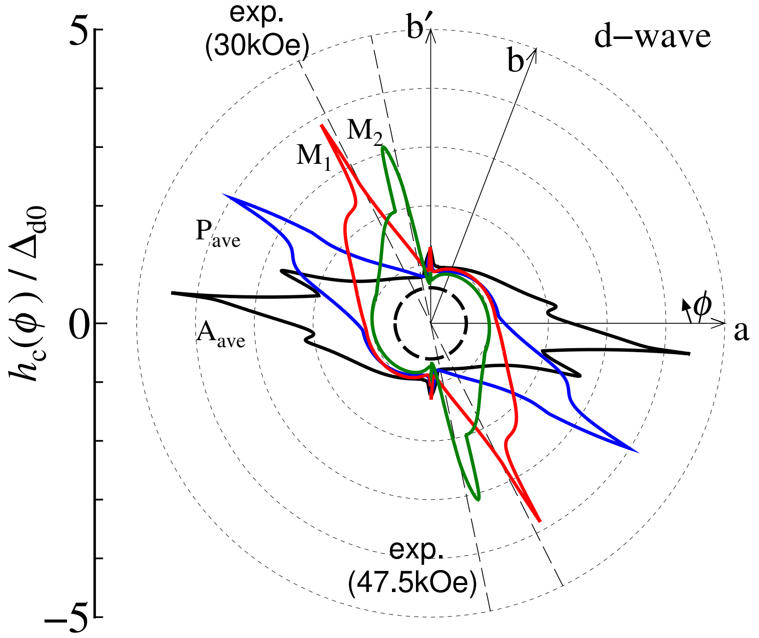

Figure 6.2: Magnetic field angular dependence of the upper critical field $h_c(\phi)$ for the d-wave state at $T = 0$. The definitions of the curves are the same as in Fig. 6.1, except for the pairing symmetry and the values of the Pauli paramagnetic limit h_P/Δ_{d0} derived from Eq. (2.8), which are approximately equal to 0.6096, 0.6075, 0.6063, and 0.6070 for A_{ave}, P_{ave}, M_1, and M_2, respectively. This figure is presented in Ref. [99].

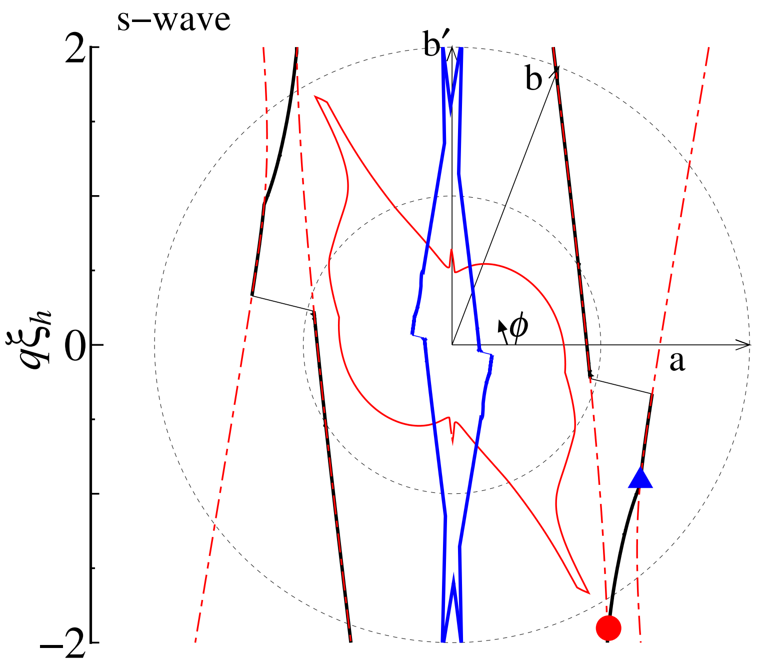

Figure 6.3: Angular dependence of optimum $q(\phi)$ for parameter set M_1. $\xi_h \equiv v_\mathrm{F}^0/2h_\mathrm{c}(\phi)$ and $v_\mathrm{F}^0 \equiv t_\mathrm{S1}t_\mathrm{S2}/\hbar\sqrt{{t_\mathrm{S1}}^2+{t_\mathrm{S2}}^2}$ are defined. v_F^0 is the Fermi velocity at the half-filling in the 1D system with $t_\mathrm{I1}=t_\mathrm{I2}=t_\mathrm{I3}=t_\mathrm{I4}=0$. The black solid curve shows the angular dependence of optimum $q(\phi)$ for the s-wave state. The blue solid curve shows the value divided by five. The red dashed curves show that the $q(\phi)$ makes the Fermi surfaces touch. The red closed circle and blue closed triangle show the optimum $q(\phi)$ at $\phi=-0.340\pi$ and $\phi=-0.199\pi$, respectively. The red solid curve shows $h_\mathrm{c}(\phi)/\Delta_\mathrm{s0}$ in an arbitrary scale.

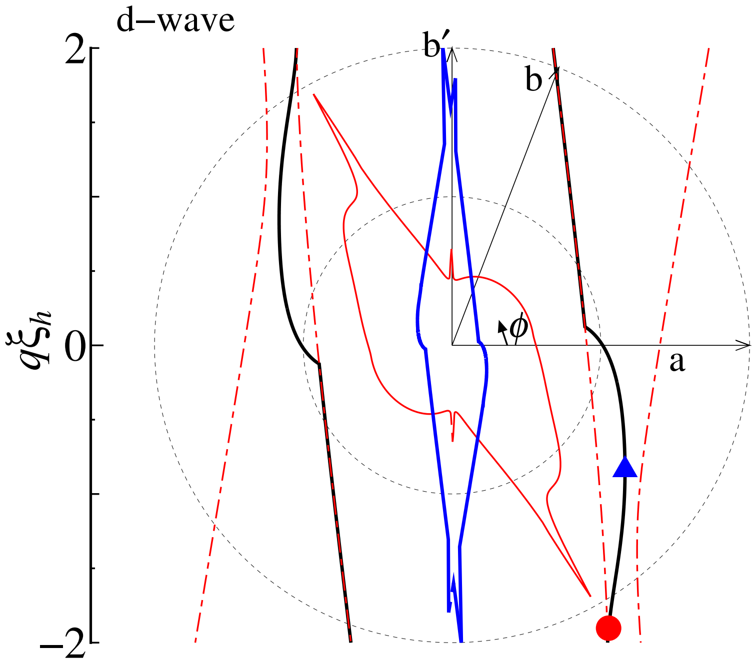

Figure 6.4: The black solid curve shows the angular dependence of optimum $q(\phi)$ for the d-wave state when parameter set M_1 is assumed. The red solid curve shows $h_\mathrm{c}(\phi)/\Delta_{\mathrm{d}0}$ in an arbitrary scale. The definitions of the other curves and points are the same as in Fig. 6.3. This figure is presented in Ref. [99].

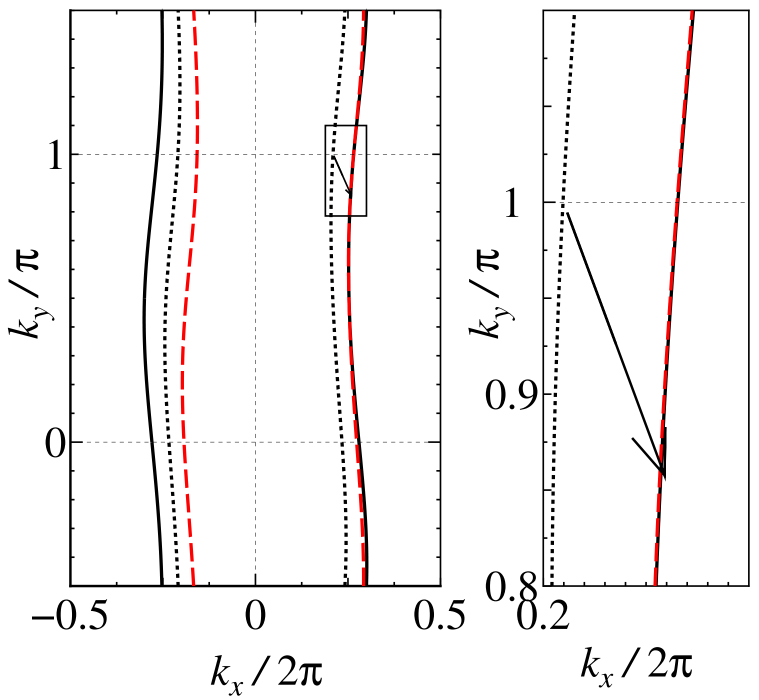

Figure 6.5: Fermi-surface nesting at $\phi = -0.340\pi$ for parameter set M_1. The upper critical field is maximum in this direction for both s- and d- wave states, and its values are $h_{\mathrm{c}}(\phi) \approx 2.860\Delta_{\mathrm{s0}}$ and $h_{\mathrm{c}}(\phi) \approx 3.925\Delta_{\mathrm{d0}}$, respectively. The black solid and dotted curves show the Fermi surfaces of up and down spins, respectively. The red dashed curve shows the Fermi surface obtained by shifting that of down spins by the vector $\boldsymbol{q}$ (the small arrows). The right panel shows a detailed figure focused on nesting. In the weak coupling theory, $h \ll t_{\mathrm{S1}}$; however, for this figure, we used a large value $h = 0.1t_{\mathrm{S1}}$ to make the displacement visible. This figure is presented in Ref. [99].

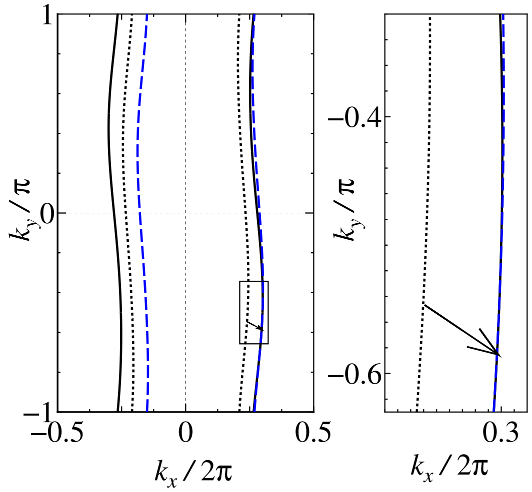

Figure 6.6: Fermi-surface nesting at $\phi = -0.199\pi$ for parameter set M_1. For the s-wave state, $h_c(\phi) \approx 1.520\Delta_{s0}$ at this ϕ. The black solid and dotted curves show the Fermi surfaces of up and down spins, respectively. The blue dashed curve shows the Fermi surface obtained by shifting that of down spins by the vector $\boldsymbol{q}$ (the small arrows). The right panel shows a detailed figure focused on nesting.

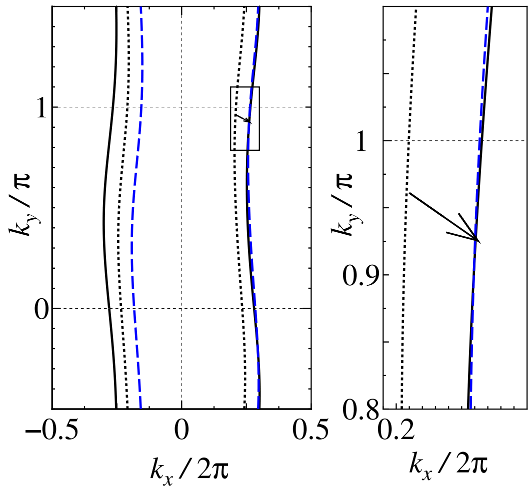

Figure 6.7: Fermi-surface nesting at $\phi = -0.199\pi$ for parameter set M_1. For the d-wave state, $h_c(\phi) \approx 1.667\Delta_{d0}$ at this ϕ. The definitions of the curves are the same as in Fig. 6.6.

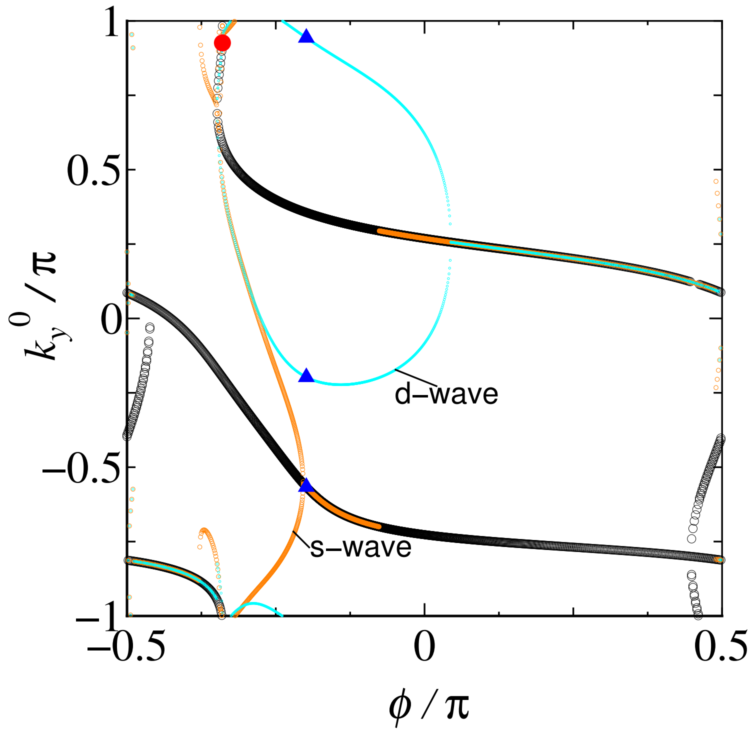

Figure 6.8: Angular dependence of the optimum nesting points k_y^0 for parameter set M_1. The black open circles show the k_y^0 that make the Fermi surfaces touch. The orange and light blue open circles show the angular dependence of the points of k_y^0 for optimum q when s- and d-wave states are assumed, respectively. The red closed circle shows the optimum k_y^0 at $\phi = -0.340\pi$. The blue closed triangles show the optimum k_y^0 at $\phi = -0.199\pi$ for s- and d-wave states, respectively.

Next, we numerically calculate Eq. (4.20) for ϕ as shown above, and examine the temperature dependence of the upper critical field $h_{\rm c}(T)$.

Figures 6.9 and 6.10 show $h_{\rm c}(T)$ for the parameter set M_1 when we assume d- and s-wave states, respectively. $h_{\rm c}(T)$ for $\phi = \phi_0 \approx -0.3392\pi$, where $n = 3$, shows a sharp up-turn at low temperatures in both s- and d-wave states. ϕ_0 is ϕ that gives the maxima of $h_{\rm c}(\phi)$, which implies the optimum direction of the magnetic field. This up-turn is different from that of $n = 2$ such as $\phi = 0.5\pi$; i.e., $\boldsymbol{H} \parallel \boldsymbol{b}'$, and $\mathrm{d}h_{\rm c}(T)/\mathrm{d}T$ at $T = 0$ for $\phi_0 \approx -0.3392\pi$ is significantly large. In contrast, for the d-wave state at $\phi = -0.199\pi$, $h_{\rm c}(T)$ does not show a up-turn near $T = 0$, and $\mathrm{d}h_{\rm c}(T)/\mathrm{d}T$ vanishes at $T = 0$ because $n = 1$ at this ϕ, which means that the Fermi surfaces cross. Thus, $\mathrm{d}h_{\rm c}(T)/\mathrm{d}T$ at $T = 0$ increases as ϕ approaches ϕ_0. This rapid increase for $\phi \approx \phi_0$ at low temperatures is similar to the behavior shown in the square lattice system for $n_{\rm h} = 0.630$, where $n = 4$ [22]. The behavior of $h_{\rm c}(T)$ at $\phi = -0.199\pi$ for the s-wave state is different from that for the d-wave state because $n = 2$, which means that the Fermi surfaces touch on a line, as mentioned above.

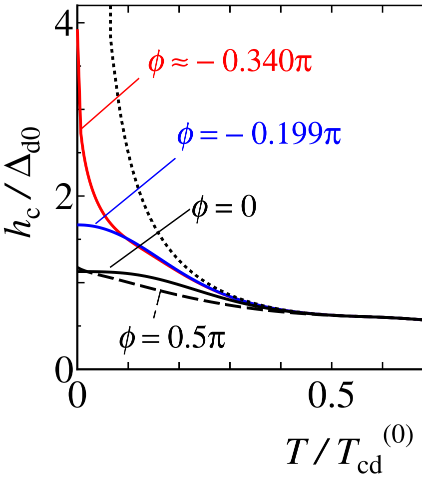

Figure 6.9: Temperature dependence of the upper critical field for parameter set M_1 when the d-wave pairing is assumed. The blue and red curves show the results for $\phi \approx -0.3392\pi$ and $\phi = -0.199\pi$, respectively. The black solid and dashed curves show the results for $\phi = 0$ and $\phi = 0.5\pi$, which means that $\boldsymbol{H} \parallel \boldsymbol{a}$ and $\boldsymbol{H} \parallel \boldsymbol{b}'$, respectively. The dotted curve shows the upper critical field in 1D systems.

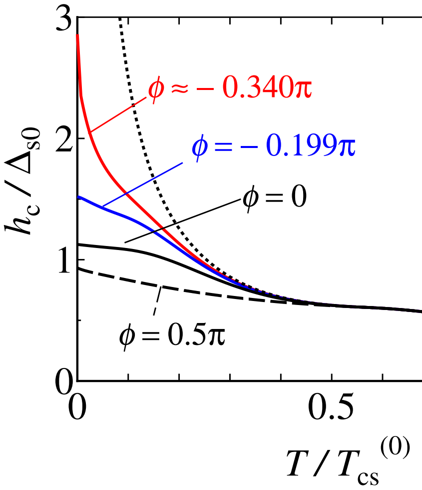

Figure 6.10: Temperature dependence of the upper critical field for parameter set M_1 when the s-wave pairing is assumed. The definitions of the curves are the same as in Fig. 6.9.

6.2 Dependence on the Fermi-surface structure

In this section, we examine the relation between the in-plane magnetic field dependence of the upper critical field $h_{\mathrm{c}}(\phi)$ and the Fermi-surface structure. As explained in the previous section, the nesting effect sensitively depends on the Fermi-surfaces structure that includes derivatives of $\epsilon(\boldsymbol{k})$ on the Fermi surface as well as the shape of the Fermi surfaces. Because the optimum direction ϕ_0 is determined by the nesting effect, even for similar appearances of the Fermi surfaces, ϕ_0 can largely differ. Therefore, only by explicit calculation of $h_{\mathrm{c}}(\phi)$ for various parameters, we can clarify their relation. In addition, we try to find the hopping integrals significant for the determination of the optimum direction.

We introduce parameters that quantitatively express the shapes of the Q1D Fermi surfaces. We define $k_{\mathrm{s}} = k_y^{(+,\mathrm{t})} - k_y^{(-,\mathrm{t})} = 2k_y^{(+,\mathrm{t})}$ and $k_{\mathrm{w}} = k_x^{(+,\mathrm{t})} - k_x^{(+,\mathrm{b})}$, which respectively express the degrees of the shear and warp of the Q1D Fermi surfaces as shown in Fig. 6.11. Here, $k_x^{(\pm,\mathrm{t})} = \pm \max_{k_y} k_x^{\mathrm{F}}(k_y)$, $k_x^{(\pm,\mathrm{b})} = \pm \min_{k_y} k_x^{\mathrm{F}}(k_y)$, and $k_y^{(\pm,\mathrm{t})}$ and $k_y^{(\pm,\mathrm{b})}$ are k_y that gives $k_x^{(\pm,\mathrm{t})}$ and $k_x^{(\pm,\mathrm{b})}$, respectively. When $k_{\mathrm{w}} = 0$, the Fermi surfaces are flat. k_{s} is a function of $\{t_{\mathrm{I}\mu} |\ \mu = 1, 2, 3, 4\}$, and has the periodicity $k_{\mathrm{s}}(\{t_{\mathrm{I}\mu}\}) = k_{\mathrm{s}}(\{-t_{\mathrm{I}\mu}\}) + 2\pi$.

We examine the relation between the optimum direction ϕ_0 and the shapes of the Fermi surfaces. Figure 6.12 shows $t_{\mathrm{S1}}/t_{\mathrm{S2}}$ dependence of ϕ_0, which implies that ϕ_0 hardly changes by $t_{\mathrm{S1}}/t_{\mathrm{S2}}$. Therefore, we fix the values of intra-chain hopping integrals t_{S1} and t_{S2}, which are 387.5 meV and 329.5 meV, respectively. The parameter sets of the inter-chain direction are sampled using a grid of $(9 \times 9 \times 9 \times 9)$ points in the $t_{\mathrm{I1}}t_{\mathrm{I2}}t_{\mathrm{I3}}t_{\mathrm{I4}}$ space, where $-0.3 \le t_{\mathrm{I1}}/t_{\mathrm{S1}} \le 0.3$, $-0.4 \le t_{\mathrm{I2}}/t_{\mathrm{S1}} \le 0.4$, $-0.3 \le t_{\mathrm{I3}}/t_{\mathrm{S1}} \le 0.3$, and $-0.15 \le t_{\mathrm{I4}}/t_{\mathrm{S1}} \le 0.15$. The optimum direction ϕ_0 is a function of $\{t_{\mathrm{I}\mu} |\ \mu = 1, 2, 3, 4\}$. Because we examine Q1D systems, we exclude the parameter sets for which the warp of the Fermi surface is so large that $k_{\mathrm{w}} > 0.20\pi$ or the Fermi surface is closed.

Figures 6.13 and 6.14 show the relation between k_{s} and ϕ_0 for the parameter sets defined above. In Fig. 6.13, the black closed circles show the points for the parameter sets with $t_{\mathrm{I}4} = 0$. For these parameter sets, the points (k_{s}, ϕ_0) are concentrated on a curve, which varies in the range of $-0.1\pi \lesssim \phi_0 \lesssim 0.1\pi$. However, as shown by the blue and red open circles, which are for the parameter sets with $t_{\mathrm{I}4} > 0$ and $t_{\mathrm{I}4} < 0$, respectively, the points (k_{s}, ϕ_0) are scattered in a wide range for $t_{\mathrm{I}4} \neq 0$. Therefore, a finite $t_{\mathrm{I}4}$ is significant for the optimum directions ϕ_0 to take various values in a wide range. The distribution of the points (k_{s}, ϕ_0) is symmetric in Fig. 6.13, because there exist both $(k_{\mathrm{s}}(\{t_{\mathrm{I}\mu}\}), \phi_0(\{t_{\mathrm{I}\mu}\}))$ and $(k_{\mathrm{s}}(\{-t_{\mathrm{I}\mu}\}), \phi_0(\{-t_{\mathrm{I}\mu}\})) + (2\pi, 0)$ in the diagram.

In Fig. 6.14, the black closed circles show the points for the parameter sets with $t_{\mathrm{I}1} = 0$. In contrast to Fig. 6.13, for these parameter sets, the points (k_{s}, ϕ_0) are not concentrated. The behavior for $t_{\mathrm{I}2}$ and $t_{\mathrm{I}3}$ are similar to that for $t_{\mathrm{I}1}$. Therefore, $t_{\mathrm{I}1}$, $t_{\mathrm{I}2}$, and $t_{\mathrm{I}3}$ are not significant for the determination of the optimum directions.

Next, we examine the relation between the optimum direction and the shapes of the Fermi surfaces. We focus on the parameter sets A_1, A_2, and A_3, which have been shown the orange triangles in Figs. 6.13 and 6.14. For these parameter sets, $k_{\mathrm{s}} \approx -\pi$ and $k_{\mathrm{w}} \approx 0.1\pi$, which implies that their Fermi surfaces are similar as shown in Fig. 6.15. However, the optimum directions ϕ_0 for these parameter sets are different, which are approximately equal to 0.191π, 0.0690π, and -0.250π, respectively, as shown in Figs. 6.13 and 6.14. Similarly, for the parameter sets B_1, B_2, and B_3 as shown by the green triangles in Figs. 6.13 and 6.14, although their Fermi surfaces are similar with $k_{\mathrm{s}} \approx -0.5\pi$ and $k_{\mathrm{w}} \approx 0.07\pi$, the optimum directions ϕ_0 are different, which are approximately 0.297π, -0.00532π, and -0.185π

respectively. For these parameters, the shapes of the Fermi surfaces are shown in Fig. 6.16. Therefore, even in the systems with similar shapes of the Fermi surfaces, the optimum directions can be different. In contrast to this behavior, the optimum directions can be similar, even when the shapes of the Fermi surfaces are completely different. In fact, the parameter sets C_1, C_2, and C_3 give different shapes of the Fermi surfaces as shown in Fig. 6.17, whereas the optimum directions ϕ_0 almost coincide ($\phi_0 \approx -0.3\pi$) as shown by the light blue triangles in Figs. 6.13 and 6.14. Therefore, the optimum direction cannot be predicted by a simple consideration for the shape of the Fermi surfaces [11].

As shown by the red closed diamonds in Figs. 6.13 and 6.14, the points for parameter sets $\mathrm{P}_{\mathrm{ave}}$, M_1, and M_2 are near the region in which the points (k_{s}, ϕ_0) are concentrated.

In Figs. 6.13 and 6.14, the points (k_{s}, ϕ_0) are not concentrated in proximately to the direction of γ. This implies that the FFLO vector cannot point this direction, in which the edge of the Fermi surfaces is open.

Figure 6.18 shows phase diagrams about values of ϕ_0 for several values of t_{I4} in the $t_{\mathrm{I2}}t_{\mathrm{I3}}$ plane when $t_{\mathrm{S1}} = 387.5$, $t_{\mathrm{S2}} = 329.5$, and $t_{\mathrm{I1}} = 50$ in the unit of meV. Also in Fig. 6.18, the behaviors as mentioned above occur. In Fig. 6.18 (a), the optimum directions ϕ_0 for the parameter sets with $t_{\mathrm{I4}} = 0$ become $-0.1\pi \lesssim \phi_0 \lesssim 0.1\pi$ in a wide range, which is expressed by a light-colored region. As the value of t_{I4} increases, a dark-colored region widen, which means that ϕ_0 variously changes. In Fig. 6.18 (b), (c), and (d), the parameter sets $\mathrm{P}_{\mathrm{ave}}$, M_1, and M_2 are included in a green-scaled region that $\phi_0 < 0$.

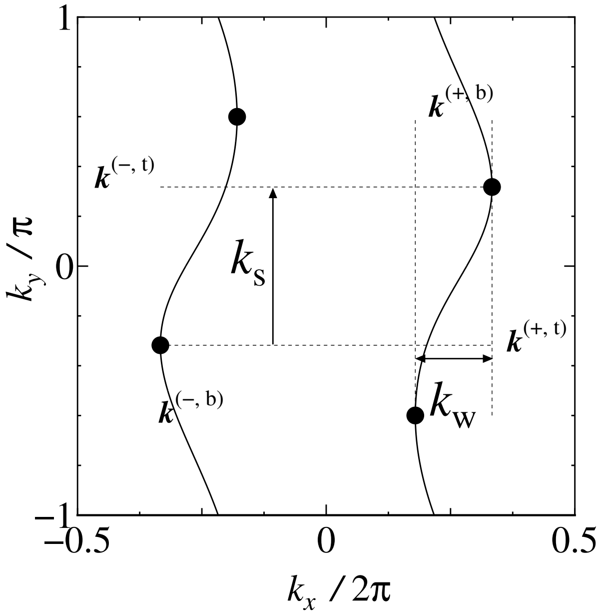

Figure 6.11: Definition of k_s and k_w. The black solid curves show the Fermi surfaces. The black closed circles show the momenta $\boldsymbol{k}^{(\pm,\mathrm{t})}$ and $\boldsymbol{k}^{(\pm,\mathrm{b})}$, which are $\boldsymbol{k}^{(\pm,\mathrm{t})} = (k_x^{(\pm,\mathrm{t})}, k_y^{(\pm,\mathrm{t})})$ and $\boldsymbol{k}^{(\pm,\mathrm{b})} = (k_x^{(\pm,\mathrm{b})}, k_y^{(\pm,\mathrm{b})})$, respectively.

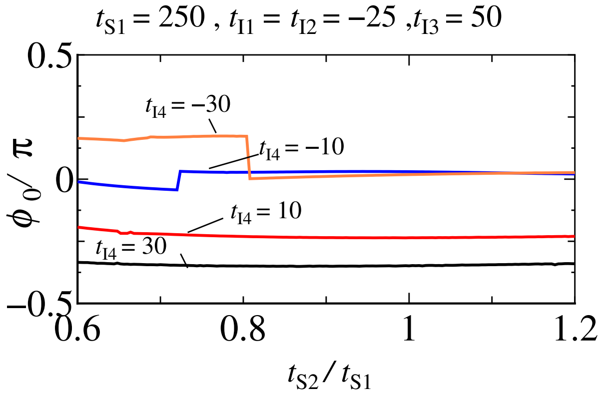

Figure 6.12: The ratio $t_{\mathrm{S2}}/t_{\mathrm{S1}}$ dependence of the optimum direction ϕ_0 for the d-wave state when $t_{\mathrm{S1}} = 250.0$, $t_{\mathrm{I1}} = t_{\mathrm{I2}} = -25.0$, and $t_{\mathrm{I3}} = 50.0$ in the unit of meV. The black, red, blue, and orange curves show the results for $t_{\mathrm{I4}} = 30.0$, 10.0, −10.0, and −30.0 in the unit of meV, respectively.

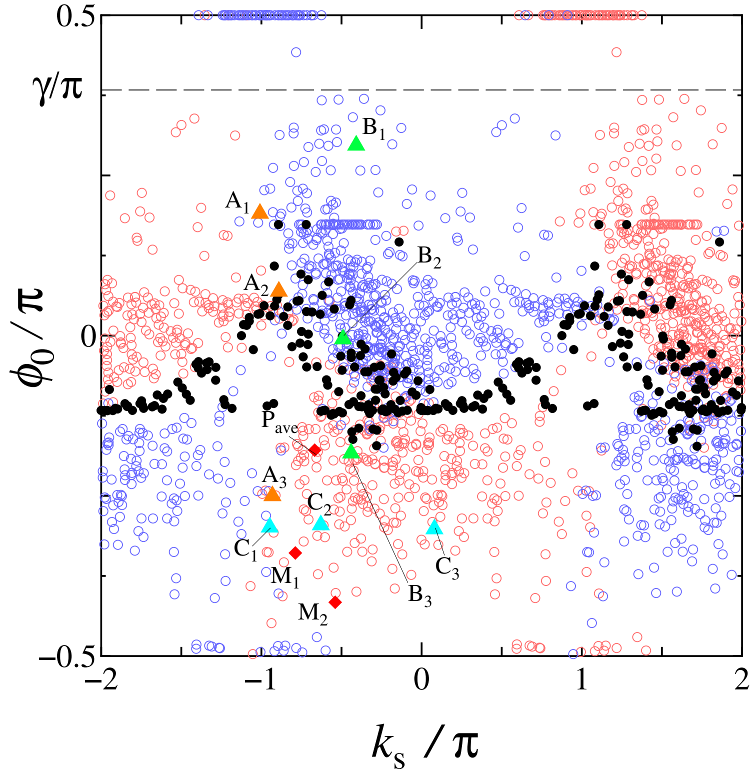

Figure 6.13: The relation between k_{s} and ϕ_0 for the d-wave state and sampled parameter sets when $t_{\mathrm{S1}} = 387.5$ meV and $t_{\mathrm{S2}} = 329.5$ meV, except for parameter sets where the edge of the Fermi surface closes. The black closed circles show the points for $t_{\mathrm{I4}} = 0$, whereas the blue and red open circles show the points for $t_{\mathrm{I4}} > 0$ and $t_{\mathrm{I4}} < 0$, respectively. The dashed straight line represents $\phi_0 = \gamma = 69.0°$, which means that $\boldsymbol{H} \parallel \boldsymbol{b}$. The red closed diamonds show the results for parameter sets $\mathrm{P}_{\mathrm{ave}}$, M_1, and M_2. The orange, green, and light blue closed triangles show the results for parameter sets A_1, A_2, and A_3, B_1, B_2, and B_3, and C_1, C_2, and C_3, respectively.

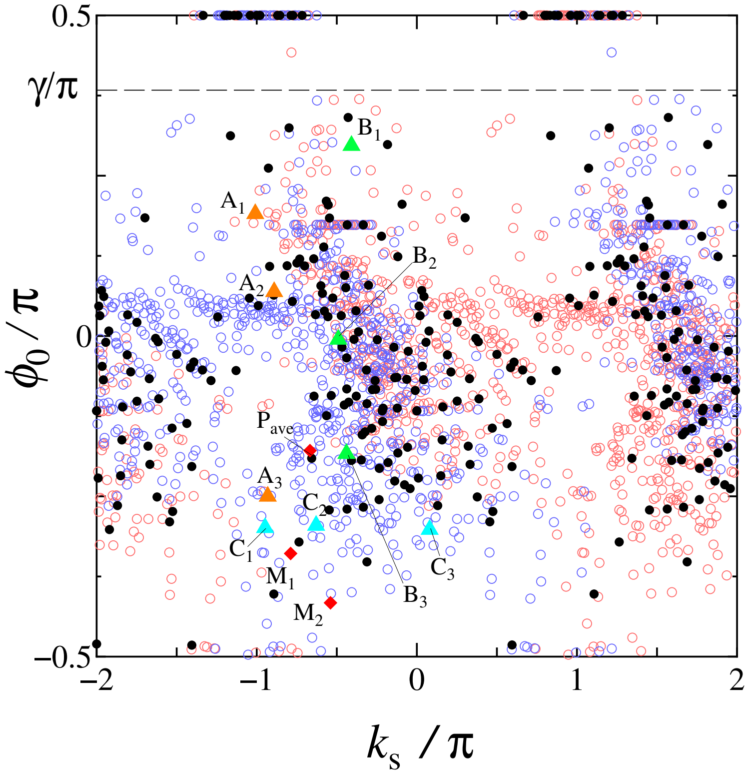

Figure 6.14: The data same as Fig. 6.13 are plotted, with different definition of the colors. The black closed circles show the points for $t_{I1} = 0$, whereas the blue and red open circles show the points for $t_{I1} > 0$ and $t_{I1} < 0$, respectively.

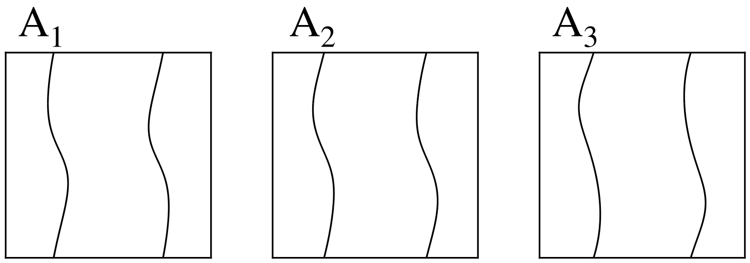

Figure 6.15: The Fermi surfaces for parameter sets A_1, A_2, and A_3, which are shown in Figs. 6.13 and 6.14. The optimum directions ϕ_0 for these parameter sets are approximately 0.191π, 0.0690π, and -0.250π, respectively.

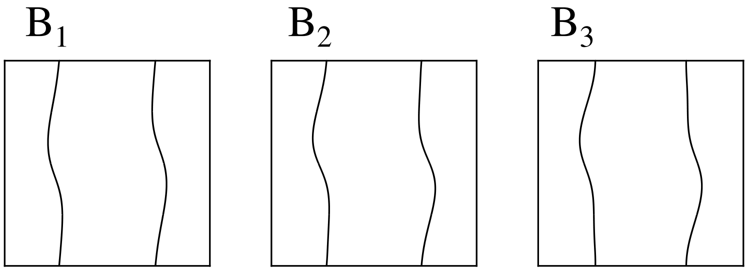

Figure 6.16: The Fermi surfaces for parameter sets B_1, B_2, and B_3, which are shown in Figs. 6.13 and 6.14. The optimum directions ϕ_0 for these parameter sets are approximately 0.297π, -0.00532π, and -0.185π, respectively.

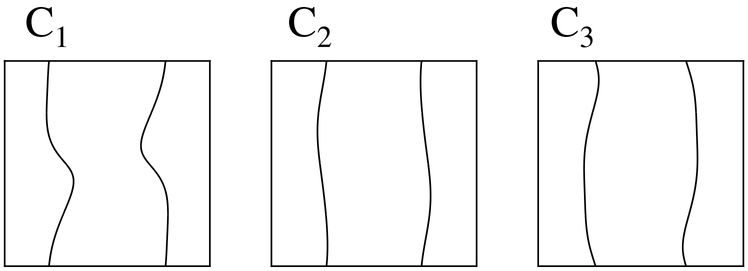

Figure 6.17: The Fermi surfaces for parameter sets C_1, C_2, and C_3, which are shown in Figs. 6.13 and 6.14. The optimum directions ϕ_0 for these parameter sets are approximately equal to -0.3π.

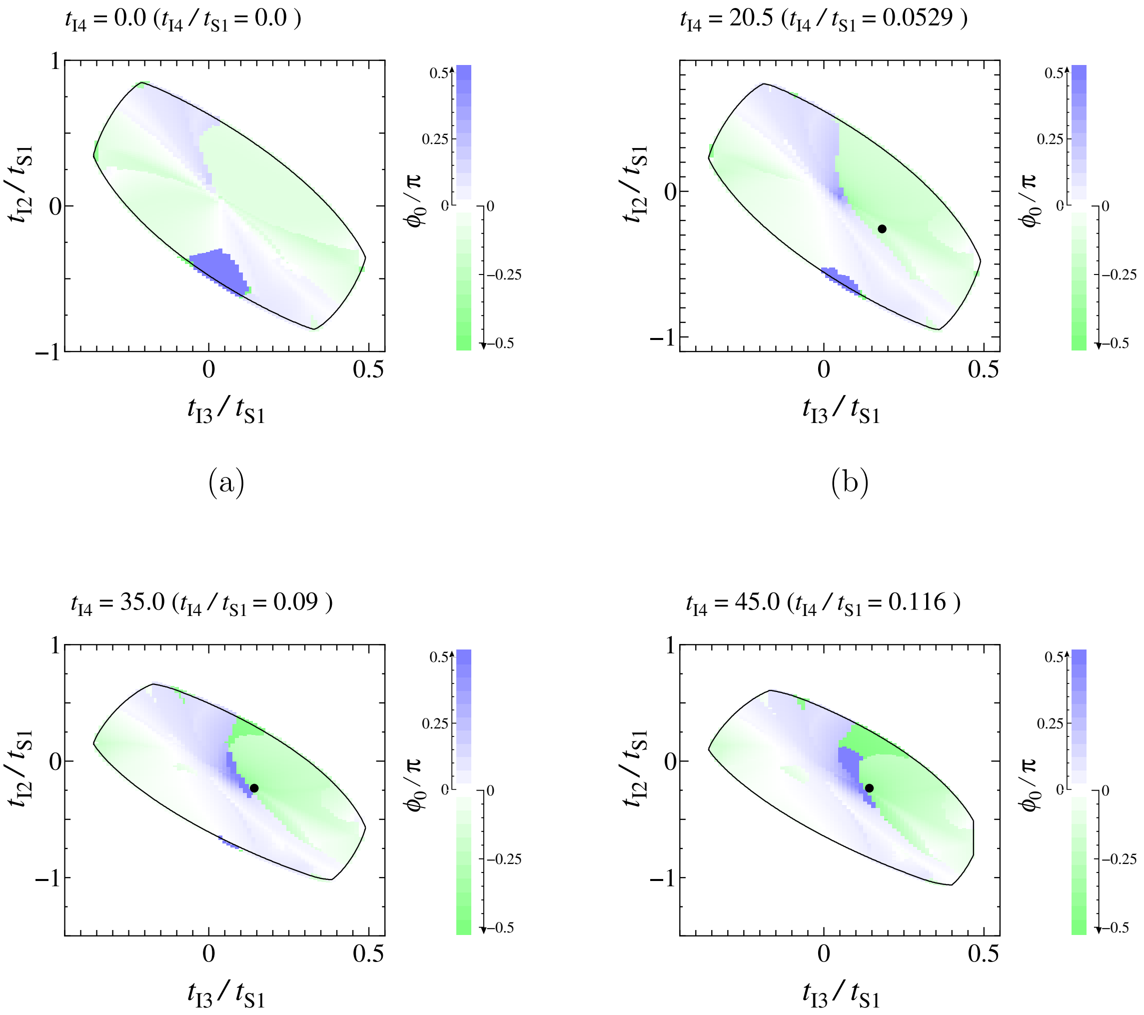

(a) (b)

(c) (d)

Figure 6.18: Phase diagrams in the $t_{I2}t_{I3}$ plane for $t_{S1} = 387.5$ meV, $t_{S2} = 329.5$ meV, $t_{I1} = -50.0$ meV, and several values of t_{I4} when the d-wave state is assumed. The color scale for the optimum direction ϕ_0/π is shown in the left panel. The solid curves are the boundaries of the area in which the Fermi surface is open. In the panels (b), (c), and (d), the closed black circles show the parameter sets P_{ave}, M_1 and M_2, respectively.

6.3 Effect of the order-parameter mixing

In this section, we numerically calculate Eq. (4.31), and examine the stability of the FFLO state in the presence of the mixing effect. As mentioned in the purpose, in Q1D organic superconductors $(\mathrm{TMTSF})_2X$, the mixing effect can occur. In the following, we examine the case that $T_{\mathrm{c}\alpha_2}^{(0)} = 0.01T_{\mathrm{c}\alpha_1}^{(0)}$, where $\alpha_1 = \mathrm{s}, \mathrm{d}$ and $\alpha_2 = \mathrm{p}, \mathrm{f}$, and assume $t_{\mathrm{S}1} = t_{\mathrm{S}2} = t_a$, $t_{\mathrm{I}3} = t_b$, and $t_{\mathrm{I}1} = t_{\mathrm{I}2} = t_{\mathrm{I}4} = 0$.

Figures 6.19 and 6.20 show $h_{\mathrm{c}}(T)$ of d- and s-wave FFLO states, respectively. In the absence of the mixing effect, the tricritical temperature $T^* \approx 0.561T_{\mathrm{c}\alpha_1}^{(0)}$ at any φ_q. In contrast, the mixing effect enhances T^*. For example, when $\alpha_1 = \mathrm{d}$ and $\alpha_2 = \mathrm{f_x}$, $T^* \approx 0.668T_{\mathrm{cd}}^{(0)}$ at $\varphi_{\boldsymbol{q}} = 0$ as shown in Fig. 6.19. The mixing effect is maximized at $\varphi_{\boldsymbol{q}} = 0$, while it does not occur at $\varphi_{\boldsymbol{q}} = \pi/2$. When $\alpha_1 = \mathrm{d}$ and $\alpha_2 = \mathrm{f_y}$, the mixing effect is maximized at $\varphi_{\boldsymbol{q}} = \pi/2$, while it does not occur at $\varphi_{\boldsymbol{q}} = 0$. For example, $T^* \approx 0.668T_{\mathrm{cd}}^{(0)}$ at $\varphi_{\boldsymbol{q}} = \pi/2$ and $T^* \approx 0.561T_{\mathrm{cd}}^{(0)}$ at $\varphi_{\boldsymbol{q}} = 0$ as shown in Fig. 6.19. In the case of the s-wave FFLO state, we obtain similar results to the d-wave FFLO state. In addition, when the mixing effect occurs, the width of the shoulder in the $h_{\mathrm{c}}(T)$, which is shown by Miyawaki and Shimahara [21], is larger than the pure FFLO state. Thus, the FFLO state is more stable because of the order-parameter mixing effect, and its stability depends on the direction of the FFLO vector and the combination of the order parameters that are mixed.

Figures 6.21 and 6.22 show $T^*(\varphi_{\boldsymbol{q}})$ for d-f and s-p mixing states, respectively. The behavior of $T^*(\varphi_{\boldsymbol{q}})$ is similar to the results as analytically shown in Section 4.4. The order-parameter mixing effect almost does not occur in d-p mixing state, and T^* almost does not enhance. When s-$\mathrm{p_x}$ and d-$\mathrm{f_x}$ mixing states occur, the tricritical temperature is maximum at $\varphi_{\boldsymbol{q}} = 0$, and decreases as the direction of $\boldsymbol{q}$ approaches $\boldsymbol{b}'$. In contrast, when s-$\mathrm{p_y}$ and d-$\mathrm{f_y}$ mixing states occur, the tricritical temperature increases as the direction of $\boldsymbol{q}$ approaches $\boldsymbol{b}'$, and is maximum at $\varphi_{\boldsymbol{q}} = \pi/2$.

Figures 6.23 and 6.24 show the ratio of hopping parameters t_b/t_a dependence of the tricritical temperature T^*. As t_b/t_a decreases, T^* increases for s-p$_\mathrm{x}$ and d-f$_\mathrm{x}$ mixing states, while T^* decreases for s-p$_\mathrm{y}$ and d-f$_\mathrm{y}$ mixing states. These behaviors remarkably appear as $\boldsymbol{q}$ approaches $\boldsymbol{b}'$.

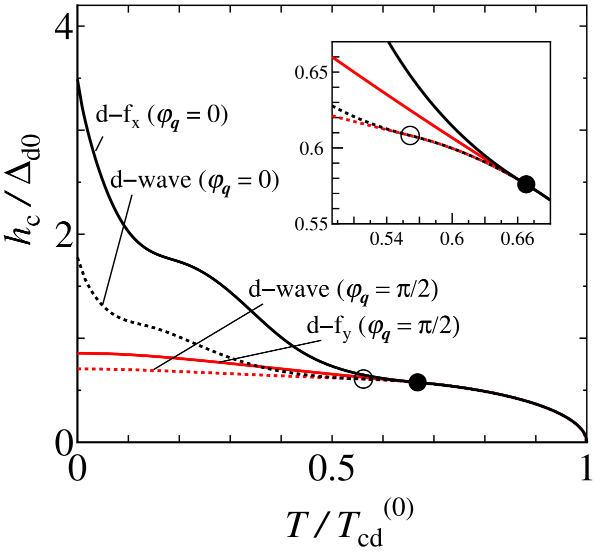

Figure 6.19: Temperature dependence of the upper critical field for the state where the d-wave pairing is dominant at $t_b/t_a = 0.10$. The black and red dotted curves show the results in the absence of the mixing effect at $\varphi_{\boldsymbol{q}} = 0$ and $\varphi_{\boldsymbol{q}} = \pi/2$, respectively. The black solid curve shows the result at $\varphi_{\boldsymbol{q}} = 0$ when $\alpha_1 = \mathrm{d}$ and $\alpha_2 = \mathrm{f_x}$. The red solid curve shows the result at $\varphi_{\boldsymbol{q}} = \pi/2$ when $\alpha_1 = \mathrm{d}$ and $\alpha_2 = \mathrm{f_y}$. The opened and closed circles show the tricritical temperature T^* in the absence and the presence of the mixing effect, respectively. The inset shows a detailed figure focused on the tricritical temperature T^*.

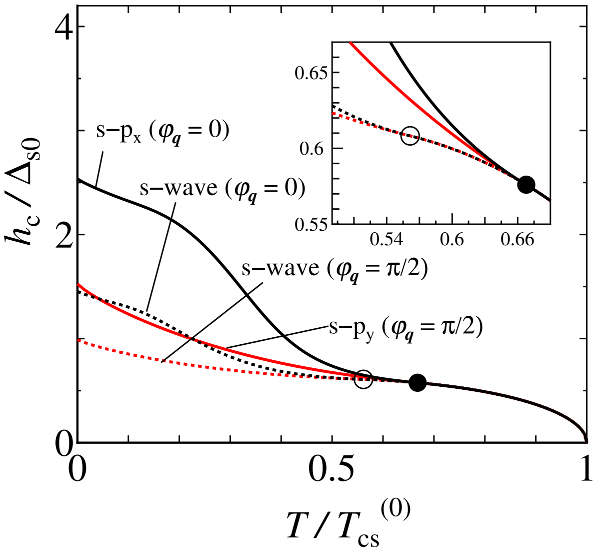

Figure 6.20: Temperature dependence of the upper critical field for the state where the s-wave pairing is dominant at $t_b/t_a = 0.10$. The black solid curve shows the result at $\varphi_{\boldsymbol{q}} = 0$ when $\alpha_1 = \mathrm{s}$ and $\alpha_2 = \mathrm{p_x}$. The red solid curve shows the result at $\varphi_{\boldsymbol{q}} = \pi/2$ when $\alpha_1 = \mathrm{s}$ and $\alpha_2 = \mathrm{p_y}$. The other curves and circles are the same as Fig. 6.19.

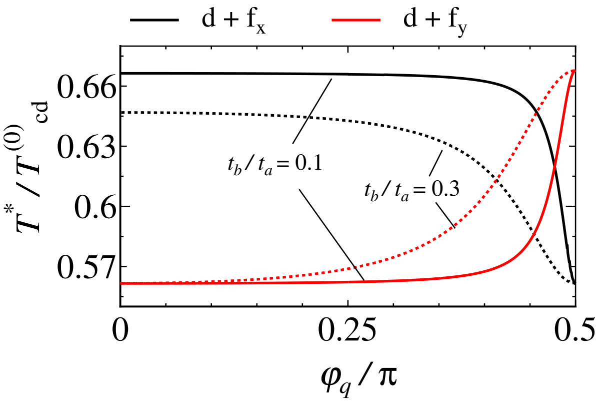

Figure 6.21: Angle $\varphi_{\boldsymbol{q}}$ dependence of the tricritical temperature. The black (red) solid and dotted curves show the results for the d-f$_x$ (d-f$_y$) mixing state at $t_b/t_a = 0.10$ and $t_b/t_a = 0.30$, respectively.

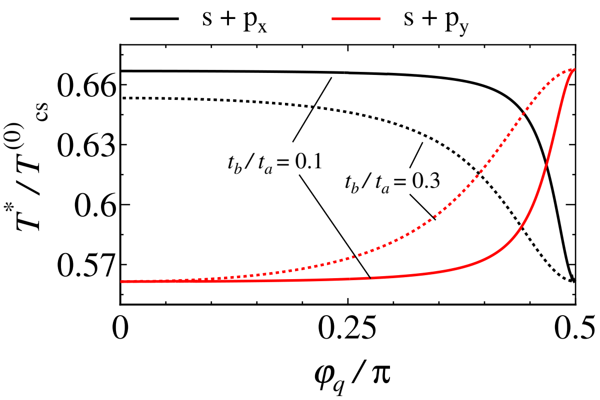

Figure 6.22: Angle $\varphi_{\boldsymbol{q}}$ dependence of the tricritical temperature. The black (red) solid and dotted curves show the results for the s-p$_x$ (s-p$_y$) mixing state at $t_b/t_a = 0.10$ and $t_b/t_a = 0.30$, respectively.

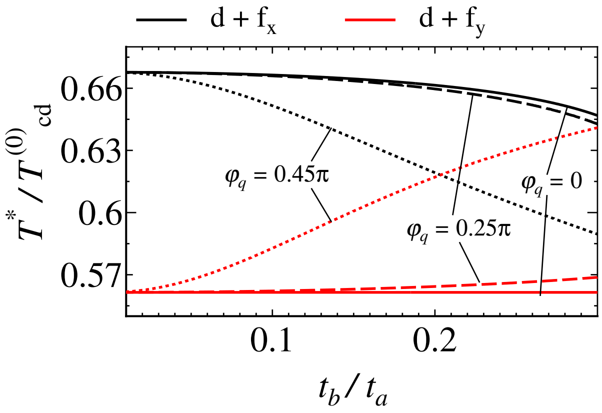

Figure 6.23: The ratio t_b/t_a dependence of the tricritical temperature. The black (red) solid, dashed, and dotted curves show the results for the d-$\mathrm{f_x}$ (d-$\mathrm{f_y}$) mixing state at $\varphi_q = 0$, $\varphi_q = 0.25\pi$, and $\varphi_q = 0.45\pi$, respectively.

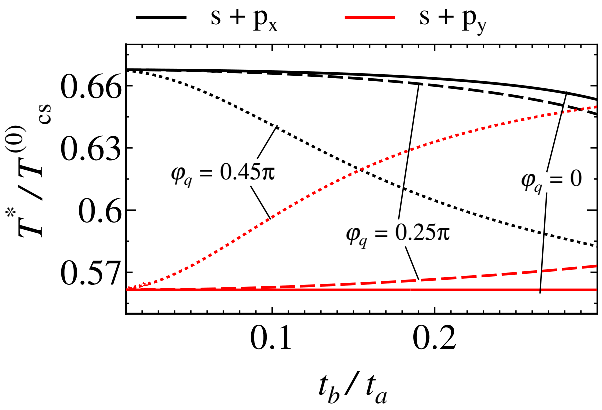

Figure 6.24: The ratio t_b/t_a dependence of the tricritical temperature. The black (red) solid, dashed, and dotted curves show the results for the s-$\mathrm{p_x}$ (s-$\mathrm{p_y}$) mixing state at $\varphi_q = 0$, $\varphi_q = 0.25\pi$, and $\varphi_q = 0.45\pi$, respectively. The red solid, dashed, and dotted curves show the results for the s-$\mathrm{p_y}$ mixing state at $\varphi_q = 0$, $\varphi_q = 0.25\pi$, and $\varphi_q = 0.45\pi$, respectively.

Chapter 7

Discussion and conclusion

In this thesis, we have studied the stability of the FFLO state in Q1D systems, particularly focused on the Fermi surface nesting effect and the order-parameter mixing effect. The observed change of the principal axis of $T_{\rm c}^{\rm onset}(\phi)$ at high fields in $({\rm TMTSF})_2{\rm ClO}_4$ is caused by the emergence of the nonzero FFLO vector $\boldsymbol{q}$. The direction of the principal axis at high fields can be determined by the nesting effect for the FFLO state, because $\boldsymbol{q} \parallel \boldsymbol{H}$ as reviewed in Chapter 2. Therefore, we have examined the Fermi surface nesting effect when the direction of the in-plane magnetic field is changed. In $({\rm TMTSF})_2X$, as reviewed in Chapter 3, in addition to the d-wave state, the triplet state has been discussed by many authors. Besides, it has been suggested that pairing interactions of singlet and triplet states coexist. Therefore, we have examined the order-parameter mixing effect. Our main results are summarized as follows.

The FFLO state is extremely stable for magnetic fields around the nontrivial optimum directions indicated by the cusps in $h_{\rm c}(\phi)$. The maximum value of $h_{\rm c}(\phi)$ at these cusps exceeds six times the Pauli paramagnetic limit. Therefore, even if the orbital pair-breaking effect is incorporated, the FFLO state can be stabilized around the optimum directions. We compared the optimum direction with the observed direction of the principal axis in $T_{\rm c}^{\rm onset}(\phi)$ at high fields. It was shown that there exist realistic parameter sets ($\rm M_1$ and $\rm M_2$) that can reproduce the optimum directions of $\boldsymbol{H}$ ($\parallel \boldsymbol{q}$) consistent with the experimental observations. Furthermore, for the parameter sets obtained from previous studies ($\rm P_{ave}$ and $\rm A_{ave}$), the optimum directions are in the quadrants consistent with the experimental observations.

The results mentioned above on the stability and the optimum direction are consistent with the hypothesis that the FFLO state emerges in $\rm (TMTSF)_2ClO_4$.

The behavior with cusps mentioned above is theoretically interesting because in the present case ϕ is controlled, whereas an analogous behavior was found in a square lattice system in which $n_{\rm h}$ is controlled to deform the Fermi surfaces [11]. Hence, a similar behavior may occur in other low-dimensional systems with other controlling parameters. This phenomenon may be universal to the FFLO state.

Now, we discuss the discrepancy between the theoretical and experimental results. For example, the present results do not coincide with the fact that the optimum direction of $\boldsymbol{H}$ depends on the magnitude of the magnetic field in the experimental $T_{\rm c}^{\rm onset}(\phi)$. The order-parameter mixing effect does not cause the temperature dependence of optimum direction ϕ_0, because ϕ_0 is primarily determined by the Fermi-surface structure. On the other hand, the orbital pair-breaking effect can cause the temperature dependence of ϕ_0 for the following reason. If vortex states with higher Landau level indices occur, the order parameter modulates in the direction perpendicular to the magnetic field [8]. Such a modulation is effectively regarded as the component of $\boldsymbol{q}$ perpendicular to $\boldsymbol{H}$. Therefore, the orbital pair-breaking effect can cause the difference between the directions $\boldsymbol{q}$ and $\boldsymbol{H}$. The orbital pair-breaking effect can cause the temperature dependence of ϕ_0 because of this difference, while when the temperature increases, the present optimum directions of $\boldsymbol{H}$ at $T = 0$ remain optimum. In addition, superconducting fluctuations may contribute to $T_{\mathrm{c}}(\phi)$ and $h_{\mathrm{c}}(\phi)$. The resistance in (TMTSF)$_2$ClO$_4$ suddenly decreases with the small width due to superconducting fluctuations as the temperature decreases, and the onset transition temperature was adopted [15]. Therefore, the observed temperature dependence of ϕ_0 can be reproduced by incorporating the effect of fluctuations.

Next, we examined whether the optimum direction ϕ_0 can be found solely by simple considerations of the shape of the Fermi surfaces. The shape of the Q1D Fermi surfaces can be crudely characterized by $(k_{\mathrm{s}}, k_{\mathrm{w}})$, which expresses the degrees of the shear and warp. We found that there is not any correlation between the optimum direction ϕ_0 and $(k_{\mathrm{s}}, k_{\mathrm{w}})$, which determines the appearance of the Fermi surfaces. The reason is that the nesting condition is determined not only by the shape of the Fermi surfaces but also by derivatives of one-particle energy $\epsilon(\boldsymbol{k})$ on the Fermi surface, such as the Fermi velocity $\boldsymbol{v}_{\mathrm{F}}(k_y)$. This behavior is analogous to the behavior found in the square lattice system [11]. In this system, $H_{\mathrm{c}}(n_{\mathrm{h}})$ for the round Fermi surface is larger than that for the Fermi surface with the flat portion.

We found that the hopping integral t_{I4} is most significant for the optimum direction ϕ_0. This result might be unexpected because t_{I4} is the second-nearest-neighbor hopping integral in the inter-chain direction, as shown in Fig. 5.1, which is smaller than the other hopping integrals. However, in the real space, the bond related to t_{I4} is as short as that related to t_{I3}, which is one of the nearest-neighbor hopping integrals.

In Q1D systems with $t_{\mathrm{S1}} = t_{\mathrm{S2}} = t_a$, $t_{\mathrm{I3}} = t_b$, and $t_{\mathrm{I1}} = t_{\mathrm{I2}} = t_{\mathrm{I4}} = 0$, we confirmed that the FFLO state is stabilized by the order-parameter mixing effect, even if the triplet order parameter is very weak, which has been shown in 2D and 3D systems [12, 13]. In Q1D organic superconductors, because the singlet and triplet pairing interactions are expected to coexist as mentioned above, this effect would be significant. For $(\alpha_1, \alpha_2) = (\mathrm{d}, \mathrm{f_x})$ and $(\mathrm{s}, \mathrm{p_x})$, the stability of the mixed state increases as the direction of $\boldsymbol{H}$ approaches a-axial direction, whereas for $(\alpha_1, \alpha_2) = (\mathrm{d}, \mathrm{f_y})$ and $(\mathrm{s}, \mathrm{p_y})$, that increases as the direction of $\boldsymbol{H}$ approaches b′-axial direction. The former mixed state is more stable when the Fermi surfaces are flat, whereas the latter mixed state is more stable when the warp of the Fermi surfaces is large. When $(\alpha_1, \alpha_2) = (\mathrm{d}, \mathrm{p_x})$ and $(\mathrm{d}, \mathrm{p_y})$, the order-parameter mixing effect does not occur. Therefore, the stability depends on the combination of α_1 and α_2, the direction of the magnetic field, and the shape of the Fermi surfaces. The behavior mentioned above can be explained by examining the dependence of $\boldsymbol{q}$ and t_b/t_a of the off-diagonal elements $M_{\alpha_1\alpha_2}$.

Our study supports the possibility that the FFLO state occurs in $(\mathrm{TMTSF})_2\mathrm{ClO}_4$. However, our study is not limited to this compound. We expect that our present results summarized above can be useful for future studies on the FFLO state in Q1D superconductors.

Appendix A

Expansion of Δk_x^{F}

In this appendix, we examine the difference between the Q1D Fermi surfaces of up and down spins expressed as

$$\Delta k_x^{\mathrm{F}}(k_y, \boldsymbol{q}) = \ k_x^{\mathrm{F}\downarrow}(k_y - q_y) - k_x^{\mathrm{F}\uparrow}(k_y) + q_x. \tag{A.1}$$

For example, $n = 3$ is shown for parameter set M_1 at $\phi_{\boldsymbol{q}} \approx -0.3392\pi$.

Equation. (A.1) is rewritten as

$$\Delta k_x^{\mathrm{F}}(k_y, \boldsymbol{q}) = k_x^{\mathrm{F}\downarrow}(k_y) - k_x^{\mathrm{F}\uparrow}(k_y) - \frac{\mathrm{d}k_x^{\mathrm{F}\downarrow}(k_y)}{\mathrm{d}k_y} q_y + q_x. \tag{A.2}$$

Because $\xi_\sigma(k_x^{\mathrm{F}\sigma}(k_y), k_y) = \sigma h$, the total derivative with respect to k_y is

$$\frac{\mathrm{d}\xi}{\mathrm{d}k_y} = \ \frac{\partial \xi}{\partial k_x} \frac{\mathrm{d}k_x^{\mathrm{F}\sigma}}{\mathrm{d}k_y} + \frac{\partial \xi}{\partial k_y}. \tag{A.3}$$

We define

$$\begin{aligned} k_x^{\mathrm{F}(0)} &= \ \frac{(k_x^{\mathrm{F}\uparrow}(k_y) + k_x^{\mathrm{F}\downarrow}(k_y))}{2}, \\ \Delta k_x^{\mathrm{F}(0)} &= \ k_x^{\mathrm{F}\downarrow}(k_y) - k_x^{\mathrm{F}\uparrow}(k_y). \end{aligned} \tag{A.4}$$

The ξ_σ is rewritten as

$$\xi(k_x^{\mathrm{F}(0)}, k_y) + \frac{\partial \xi}{\partial k_x} \frac{1}{2} \sigma \Delta k_x^{\mathrm{F}(0)} = \ \sigma h. \tag{A.5}$$

From Eqs. (A.3) and (A.5), we obtain

$$\begin{aligned}\Delta k_x^{\mathrm{F}}(k_y, \boldsymbol{q}) &= \Delta k_x^{\mathrm{F}(0)} - \frac{dk_x^{\mathrm{F}\downarrow}(k_y)}{dk_y} q_y - q_x \\ &= \frac{2h}{v_{\mathrm{F}x}} - \left.\frac{v_{\mathrm{F}y}}{v_{\mathrm{F}x}}\right|_{(k_x^{\mathrm{F}\sigma}, k_y)} q_y - q_x,\end{aligned} \tag{A.6}$$

where $v_{\mathrm{F}x} \equiv \partial\xi/\partial k_x$, and $v_{\mathrm{F}y} \equiv \partial\xi/\partial k_y$. Therefore, at k_y^0,

$$2h = \boldsymbol{q} \cdot \boldsymbol{v}_{\mathrm{F}}(s, k_y). \tag{A.7}$$

We expand $\Delta k_x^{\mathrm{F}}(k_y, \boldsymbol{q})$ as

$$\Delta k_x^{\mathrm{F}}(k_y, \boldsymbol{q}) = \sum_{k=1}^{\infty} C_k (k_y - k_y^0(\boldsymbol{q}))^k, \tag{A.8}$$

where

$$C_k = \frac{1}{k!} \left.\frac{\partial^k \Delta k_x^{\mathrm{F}}(k_y, \boldsymbol{q})}{\partial^k k_y}\right|_{k_y = k_y^0(\boldsymbol{q})}. \tag{A.9}$$

When C_k with $k = 1, 2 \cdots n-1$ vanish, we obtain $\Delta k_x^{\mathrm{F}}(k_y, \boldsymbol{q}) \propto (k_y - k_y^0(\boldsymbol{q}))^n$ for small $(k_y - k_y^0(\boldsymbol{q}))$.

When parameter set M_1 is assumed, we obtain $n = 3$ for the optimum $\phi_{\boldsymbol{q}} \approx -0.3392\pi$ (i.e., $\varphi_{\boldsymbol{q}} \approx -0.3070\pi$), $|\boldsymbol{q}| \approx 5.216 h_{\mathrm{c}}/t_{\mathrm{S1}}$, and $k_y^0 \approx 0.9570\pi$ from numerical calculation. The red dashed curves in Figs. 6.3 and 6.4 are obtained from the condition $C_1 = 0$.

Appendix B

Detailed explanation of Tab. 4.1

In this appendix, we analytically calculate the magnitude of the mixing effect.

In the weak coupling limit, the off-diagonal elements in Eq. (4.31) are

$$M_{\alpha_1\alpha_2} = \frac{1}{N}\sum_{\boldsymbol{k}} \gamma_{\alpha_1}(\boldsymbol{k})\gamma_{\alpha_2}(\boldsymbol{k}) \sum_{\sigma} \frac{1}{2\xi} \tanh\left(\frac{(\xi+\sigma\zeta)}{2T}\right). \tag{B.1}$$

$M_{\alpha_1\alpha_2}$ is expanded as $M_{\alpha_1\alpha_2} = \sum_{k_1} M^{(k_1)}_{\alpha_1\alpha_2} q^{k_1}$. Here, we define

$$M^{(k_1)}_{\alpha_1\alpha_2} = \sum_{s=\pm}\int_{-\pi}^{\pi} \frac{\mathrm{d}k_y}{2\pi}\rho(0,k_y)\gamma_{\alpha_1}(\boldsymbol{k})\gamma_{\alpha_2}(\boldsymbol{k}) x^{k_1}(k_y,\varphi_{\boldsymbol{q}},s)\int_{-\omega_{\mathrm{D}}}^{\omega_{\mathrm{D}}} \mathrm{d}\xi L^{(k_1)}(\xi), \tag{B.2}$$

where

$$L^{(k_1)}(\xi) = \frac{1}{k_1!}\left[\frac{\partial^{k_1}}{\partial \xi^{k_1}}\sum_{\sigma}\tanh\left(\frac{(\xi+\sigma\zeta)}{2T}\right)\right], \tag{B.3}$$

$\rho(0,k_y) = 1/[4\pi\sin(k_x^{\mathrm{F}}(k_y))]$, and

$$x(k_y,\varphi_{\boldsymbol{q}},s) = \sin(sk_x^{\mathrm{F}}(k_y))\cos\varphi_{\boldsymbol{q}} + t_b\sin(k_y)\sin\varphi_{\boldsymbol{q}}. \tag{B.4}$$

We have defined $t_a = 1$. Further, we expand the term depending on $k_x^{\mathrm{F}}(k_y)$. For example,

$$\sum_{k_2=0}^{\infty}\frac{\partial^{k_2}k_x^{\mathrm{F}}(k_y)}{\partial {t_b}^{k_2}} = C_0 + C_1\cos(k_y)t_b + \mathcal{O}({t_b}^2), \tag{B.5}$$

$$\sum_{k_2=0}^{\infty} \frac{\partial^{k_2} \rho(0, k_y)}{\partial {t_b}^{k_2}} = \frac{1}{\sin C_0} - \frac{\cos{(C_0)}}{\sin^2{(C_0)}} C_1 \cos{(k_y)} t_b + \mathcal{O}({t_b}^2), \tag{B.6}$$

and

$$\sum_{k_2=0}^{\infty} \frac{\partial^{k_2} \sin{(k_x^{\mathrm{F}}(k_y))}}{\partial {t_b}^{k_2}} = \sin C_0 + \cos{(C_0)} C_1 \cos{(k_y)} t_b + \mathcal{O}({t_b}^2), \tag{B.7}$$

where $C_0 = \arccos{(-\frac{\mu}{2})}$ and $C_1 = 2/\sqrt{4-\mu^2}$. Therefore, $M_{\alpha_1\alpha_2}$ is expanded as

$$M_{\alpha_1\alpha_2} = \sum_{k_1, k_2} M_{\alpha_1\alpha_2}^{(k_1,k_2)} q^{k_1} {t_b}^{k_2}. \tag{B.8}$$

When $M_{\alpha_1\alpha_2}^{(k_1,k_2)}$ with $k_1 = 0, 1, \cdots m-1$ and $k_2 = 0, 1, \cdots l-1$ vanish, we obtain $M_{\alpha_1\alpha_2} \propto q^m (t_b)^l$ for small q and t_b.

We analytically calculate the $M_{\alpha_1\alpha_2}^{(k_1,k_2)}$ except for the term depending on ξ. For example, when $\alpha_1 = \mathrm{s}$ and $\alpha_2 = \mathrm{p_x}$, $m = 1$ and $l = 0$ at $\varphi_{\boldsymbol{q}} = 0$, while $M_{\alpha_1\alpha_2}^{(k_1,k_2)} = 0$ for any k_1 and k_2 at $\varphi_{\boldsymbol{q}} = \pi/2$. When $\alpha_1 = \mathrm{d}$ and $\alpha_2 = \mathrm{p_x}$, $m = 3$ and $l = 1$ at $\varphi_{\boldsymbol{q}} = 0$, while $M_{\alpha_1\alpha_2}^{(k_1,k_2)} = 0$ for any k_1 and k_2 at $\varphi_{\boldsymbol{q}} = \pi/2$.

Reference

[1] R. Casalbuoni and G. Nardulli, Rev. Mod. Phys. **76**, 263 (2004).

[2] Y. Matsuda and H. Shimahara, J. Phys. Soc. Jpn. **76**, 051005 (2007).

[3] H. Shimahara, in *The Physics of Organic Superconductors and Conductors*, ed. A.G. Lebed (Springer, Berlin, 2008), p. 687.

[4] P. Fulde and R. A. Ferrell, Phys. Rev. **135**, A550 (1964).

[5] A. I. Larkin and Yu. N. Ovchinnikov, Zh. Eksp. Teor. Fiz. **47**, 1136 (1964); translation: Sov. Phys. JETP, **20**, 762 (1965).

[6] S. Takada and T. Izuyama, Prog. Theor. Phys. **53**, 635 (1969)

[7] L. G. Aslamazov Zh. Eksp. Teor. Fiz. **55**, 1477 (1968); translation: Sov. Phys. JETP **28**, 773 (1969).

[8] H. Shimahara and D. Rainer, J. Phys. Soc. Jpn. **66**, 3591 (1997).

[9] H. Shimahara, Phys. Rev. B **50**, 12760 (1994).

[10] H. Shimahara, J. Phys. Soc. Jpn. **66**, 541 (1997).

[11] H. Shimahara, J. Phys. Soc. Jpn. **68**, 3069 (1999); J. Supercond. **12**, 469 (1999).

[12] S. Matsuo, H. Shimahara and K. Nagai, J. Phys. Soc. Jpn **63**, 2499 (1994).

[13] H. Shimahara, Phys. Rev. B **62**, 3524 (2000).

[14] S. Yonezawa, S. Kusaba, Y. Maeno, P. Auban-Senzier, C. Pasquier, K. Bechgaard, and D. Jerome, Phys. Rev. Lett. **100**, 117002 (2008).

[15] S. Yonezawa, S. Kusaba, Y. Maeno, P. Auban-Senzier, C. Pasquier, and D. Jerome, J. Phys. Soc. Jpn. **77**, 054712 (2008).

[16] L. W. Gruenberg and L. Gunther, Phys. Rev. Lett. **16**, 996 (1996).

[17] Y. Suginishi and H. Shimahara, J. Phys. Soc. Jpn. **73**, 11 (2004).

[18] H. Shimahara, J. Phys. Soc. Jpn. **58**, 1735 (1989).

[19] H. Shimahara, J. Phys. Soc. Jpn. **69**, 1966 (2000).

[20] A. M. Clogston, Phys. Rev. Lett. **9**, 266 (1962); B. S. Chandrasekhar, Appl. Phys. Lett. **1**, 7 (1962).

[21] N. Miyawaki and H. Shimahara, J. Phys. Soc. Jpn. **83**, 024703 (2014).

[22] H. Shimahara and K. Moriwake, J. Phys. Soc. Jpn. **71**, 1234 (2002).

[23] H.Shimahara and S.Hata, Phys. Rev. B **62**, 14541 (2000).

[24] Saint-James, D., G. Sarma, and E. J. Thomas, 1969, *Type-II Superconductivity*, (Pergamon, Oxford, England).

[25] D. Jerome, Mol. Cryst. Liq. Cryst. **79**, 155 (1982).

[26] L. Balicas, J. S. Brooks, K. Storr, S. Uji, M. tokumoto, H. Tanaka, H. Kobayashi, A. Kobayashi, V. Barzykin, and L. P. Gor'kov Phys. Rev. Lett **87**, 067002 (2001).

[27] J. Singleton, J. A. Symington, M.-S. Nam, A. Ardavan, M. Kurmoo, and P. Day, J. Phys. Condens. Matter **12**, L641 (2000).

[28] R. Lortz, Y. Wang, A. Demuer, P. H. M. Böttger, B. Bergk, G. Zwicknagl, Y. Nakazawa, and J. Wosnitza, Phys. Rev. Lett. **99**, 187002 (2007).

[29] B. Bergk, A. Demuer, I. Sheikin, Y. Wang, J. Wosnitza, Y. Nakazawa, and R. Lortz, Phys. Rev. B **83**, 064506 (2011).

[30] Charles C. Agosta, Nathnael A. Fortune, Scott T. Hannahs, Shuyao Gu, Lucy Liang, Ju-Hyun Park, and John A. Schleuter, Phys. Rev. Lett. **4118**, 267001 (2017).

[31] J. A. Wright, E. Green, P. Kuhns, A. Reyes, J. Brooks, J. Schlueter, R. Kato, H. Yamamoto, M. Kobayashi, and S. E. Brown, Phys. Rev. Lett. **107**, 087002 (2011).

[32] H. Mayaffre, S. Krämer, M. Horvatic, C. Berthier, K. Miyagawa, K. Kanoda, and V.F. Mitrovic, Nphys. **3121**, 101038 (2014).

[33] S. Uji, T. Terashima, M, Nishimura, Y. Takahide, T. Konoike, K. Enomoto, H. Cui, H. Kobayashi, A. Kobayashi, H. Tanaka, M. Tokumoto, E. S. Choi, T. Tokumoto, D. Graf, and J. S. Brooks, Phys. Rev. Lett **97**, 157001 (2006).

[34] S. Uji, K. Kodama, K. Sugii, T. Terashima, Y. Takahide, N. Kurita, S. Tsuchiya, M. Kimata, A. Kobayashi, B. Zhou, and H. Kobayashi, Phys. Rev. B **85**, 174530 (2012).

[35] H. Shimahara, J. Phys. Soc. Jpn. **71**, 1644 (2002).

[36] M. A. Tanatar, T. Ishiguro, H. Tanaka, and H. Kobayashi, Phys. Rev. B **66**, 134503 (2002).

[37] S. Uji, Y. Iida, S. Sugiura, T. Isono, K. Sugii, N. Kikugawa, T. Terashima, S. Yasuzuga, H. Akutsu, Y. Nakazawa, D. Graf, P. Day, Phys. Rev. B **97**, 144505 (2018).

[38] K. Cho, B. E. Smith, W. A. Coniglio, L. E. Winter, C. Agosta, and J. A. Schlueter, Phys. Rev. B **79**, 220507(R) (2009).

[39] T. Ishiguro, K. Yamaji, and G. Saito, *Organic Superconductors* (Springer, Berlin, 1998), 2nd ed.

[40] K. Andres, F. Wudl, D. B. McWhan, G. A. Thomas, D. Nalewajek, and A. L. Stevens, Phys. Rev. Lett **45**, 1449 (19080).

[41] I. J. Lee, A. P. Hope, M. J. Leone, and M. J. Naughton, Synth. Met. **70**, 747 (1995).

[42] I. J. Lee, M. J. Naughton, G. M. Danner, and P. M. Chaikin, Phys. Rev. Lett. **78**, 3555 (1997).

[43] I. J. Lee, P. M. Chaikin, and M. J. Naughton, Phys. Rev. B **62**, 14669(R) (2000).

[44] P. Alemany, J.-P. Pouget, and E. Canadell, Phys. Rev. B **89**, 155124 (2014).

[45] D. Le Pévelen, J. Gaultier, Y.Barrans, D. Chasseau, F. Castet, and L. Ducasse, Eur. Phys. J. B **19**, 363 (2001)

[46] S. Kusaba, S. Yonezawa, Y. Maeno, P. Auban-Senzier, C. Pasquier, K .Bechgaard, and D. Jérome, Solid State Sci. **10**, 1768 (2008)

[47] N. Miyawaki and H. Shimahara, J. Phys.: Conf. Ser. **702**, 012002 (2016).

[48] Y. Hasegawa and H. Fukuyawa, J. Phys. Soc. Jpn. **56**, 877 (1987).

[49] M. Takigawa, H. Yasuoka, and G. Saito, J. Phys. Soc. Jpn. **56**, 873 (1987).

[50] J. Shinagawa, Y. Kurosaki, F. Zhang, C. Parker, S. E. Brown, D. Jérome, J. B. Christensen, K. Bechgaard, Phys. Rev. Lett. **98**, 147002 (2007).

[51] S. Yonezawa, Y. Maeno, K. Bechgaard, and D. Jérome, Phys. Rev. B **85**, 140502(R) (2012).

[52] S. Yonezawa, Y. Maeno, K. Bechgaard, and D. Jérome, Journal of Phys. **449**, 012032 (2013).

[53] S. Belin and K. Behnia, Phys. Rev. Lett. **79**, 2125 (1997).

[54] I. J. Lee, S. E. Brown, W. G. Clark, M. J. Strouse, M. J. Naughton, W. Kang, and P. M. Chaikin, Phys. Rev. Lett. **88**, 017004 (2001).

[55] J.I. Oh and M.J. Naughton, Phys. Rev. Lett. **92**, 067001 (2004).

[56] Y. Tanaka and K. Kuroki, Phys. Rev. B. **70**, 060502 (2004).

[57] K. Kuroki and Y. Tanaka, J. Phys. Soc. Jpn. **74**, 6 (2005).

[58] K. Kuroki, R. Arita and H. Aoki, J. Phys. Soc. Jpn. **63**, 094509 (2001).

[59] K. Kuroki, Y. Tanaka, T. Kumura and R. Arita, Phys. Rev. B **69**, 214511 (2004).

[60] J. C. Nickel, R. Cuprat, C. Bourbonnais and N. Dupuis, Phys. Rev. Lett. **95**, 247001 (2005).

[61] K. Fukui and Y. Kato, J. Phys. Soc. Jpn. **87**, 014706 (2018).

[62] A. I. Buzdin and H. Kachakchi, Physics. Letters. A. **225**, 341 (1997).

[63] A. I. Buzdin, Physica B. **407**, 1912 (2012)

[64] N. Dupuis, Phys. Rev. B **51**, 9074 (1995).

[65] N. Dupuis and G. Montambaux, Phys. Rev. B **49**, 8993 (1994).

[66] N. Dupuis, G. Montambaux, and C. A. R. Sá de Melo, Phys. Rev. Lett. **70**, 2613 (1993).

[67] M. Shahbazi, Y. Fuseya, H. Bakrim, A. Sedeki, and C. Bourbonnais, Phys. Rev. B **95**, 165111 (2017).

[68] A.G. Lebed and S. Wu, Phys. Rev. B **82**, 172504 (2010).

[69] M.D. Croitoru, M. Houzet, and A.I. Buzdin, Phys. Rev. Lett. **108**, 207005 (2012).

[70] M.D. Croitoru, M. Houzet, and A.I. Buzdin, J. Supercond. Nov. Magn. **25**, 1283 (2012)

[71] M. D. Croitoru and A. I. Buzdin, J. Supercond. Nov. Magn. **26**, 1657 (2013)

[72] M. D. Croitoru and A. I. Buzdin, J. Supercond. Nov. Magn. **28**, 1305 (2015)

[73] M. D. Croitoru and A. I. Buzdin, Phys. Rev. B **94**, 241512 (2016).

[74] M. Miyazaki, K. Kishigi, and Y. Hasegawa, J. Phys. Soc. Jpn. **68**, 3794 (1999).

[75] H. Aizawa, K. Kuroki, T. Yokoyama, and Y. Tanaka, Phys. Rev. Lett. **102**, 016403 (2009).

[76] H. Aizawa, K. Kuroki, T. Yokoyama, and Y. Tanaka, J. Phys. Soc. Jpn. **78**, 124711 (2009).

[77] L. P. Gor'kov, J. Exptl. Theoret. Phys. (U.S.S.R.) **37**, 833 (1989); translation: Sov. Phys. JETP **37**, 593 (1960).

[78] K. Maki and H. Won, Physica (Amsterdam) **322B**, 315 (2002).

[79] A. G. Lebed, Phys. Rev. B **97**, 144504 (2018).

[80] H. Shimahara, S. Matsuo, K. Nagai, Phys. Rev. B **53**, 12284 (1995).

[81] L.N. Bulaevskii, Zh. Eksp. Teor. Fiz. **65**, 1278 (1973); translation: Sov. Phys. JETP **38**, 634 (1974).

[82] A. I. Buzdin and J. P. Brison, Physics. Letter. A. **218**, 359 (1996).

[83] A. G. Lebed, Phys. Rev. B **59**, R721 (1999).

[84] H. Shimahara, Phys. Rev. B **80**, 214512 (2009).

[85] E. Helfand and N. R. Werthamer, Phys. Rev. Lett. **13**, 686 (1964).

[86] E. Helfand and N. R. Werthamer, Phys. Rev. **147**, 288 (1966).

[87] K. Scharnberg and R. A. Klemm, Phys. Rev. B **22**, 5233 (1980).

[88] H. Schwenk, E. Hess, K. Andres, F. Wudl and E. Aharon-Shalom, Phys. Lett. A **102**, 57 (1984)

[89] H. Shimahara, cond-mat/0403628

[90] A. A. Abrikosov, Physica C **222**, 191 (1994).

[91] A. A. Abrikosov, Physica C **244**, 243 (1995).

[92] H. Shimahara and M. Kohmoto, Europhys. Lett. **56**, 736 (2002).

[93] H. Shimahara and M. Kohmoto, Phys. Rev. B **65**, 174502 (2002).

[94] D. J. Scalpino, E. Loh. Jr. and J. E. Hirsch, Phys. Rev. B **34**, 8190 (1986).

[95] H. Shimahara and S. Takada, J. Phys. Soc. Jpn. **57**, 1044 (1988).

[96] T. Nomura and K. Yamada, J. Phys. Soc. Jpn. **70**, 2694 (2001).

[97] H. Shimahara, J. Phys. Soc. Jpn. **67**, 736 (1998).

[98] K. Kishigi and Y. Hasegawa, Phys. Rev. B **94**, 085405 (2016).

[99] K. Itahashi and H. Shimahara, J. Phys. Soc. Jpn. **87**, 083701 (2018).